

Constraints on New Physics with Light Mediators and Generalized Neutrino Interactions via Coherent Elastic Neutrino Nucleus Scattering

S. Karadağ,^{1,2,*} M. Deniz,^{3,†} S. Karmakar,^{2,4} M. K. Singh,^{2,5} M. Demirci,⁶ Greeshma C.,^{2,7} H. B. Li,² S. T. Lin,⁸ M. F. Mustamin,⁶ V. Sharma,⁹ L. Singh,⁷ M. K. Singh,⁴ V. Singh,⁷ and H. T. Wong²
(The TEXONO Collaboration)

¹*Department of Physics Engineering, Istanbul Technical University, Sarıyer, İstanbul TR34467, Türkiye*

²*Institute of Physics, Academia Sinica, Taipei 11529*

³*Department of Physics, Dokuz Eylül University, Buca, İzmir TR35160, Türkiye*

⁴*Department of Physics, Institute of Applied Sciences and Humanities, GLA University, Mathura 281406, India*

⁵*Department of Physics, Institute of Science, Banaras Hindu University, Varanasi 221005, India*

⁶*Department of Physics, Karadeniz Technical University, TR61080 Trabzon, Türkiye*

⁷*Department of Physics, School of Physical and Chemical Sciences, Central University of South Bihar, Gaya 824236, India*

⁸*College of Physics, Sichuan University, Chengdu 610065*

⁹*Department of Physics, H.N.B. Garhwal University, Srinagar 246174, India*

(Dated: February 28, 2025)

We investigate new physics effects on the framework of Coherent Elastic Neutrino Nucleus Scattering (CE ν NS) from Non-Standard Interactions (NSI) of neutrinos and generalized neutrino interactions (GNI) as well as the possibility of light mediators from simplified model which includes all possible Lorentz-invariant interactions of vector (V), axialvector (A), scalar (S), pseudoscalar (P), and tensor (T) type. The constraints and the allowed regions at 90% C. L. for masses and couplings in each new physics scenario are derived from the analysis of TEXONO data, including two datasets from 2016 with a high purity n -type point-contact (nPC) germanium (Ge) detector and from 2024 with an advanced p -type point-contact (pPC) Ge detector. The results are presented in comparison with the current data of COHERENT with CsI and LAr detectors to highlight the complementarity of reactor- and accelerator-based neutrino experiments.

I. INTRODUCTION

Neutrino interactions with matter [1] have long been considered as promising avenues for uncovering new physics phenomena. The neutrino-nucleus elastic (νA_{el}) scattering process [2, 3],

$$\nu_\alpha(\bar{\nu}_\alpha) + A(\mathcal{Z}, \mathcal{N}) \longrightarrow \nu_\alpha(\bar{\nu}_\alpha) + A(\mathcal{Z}, \mathcal{N}), \quad (1.1)$$

where α stands for lepton flavor (e , μ or τ) for incoming or outgoing neutrinos and $A(\mathcal{Z}, \mathcal{N})$ denotes the atomic nucleus, characterized by its atomic number (\mathcal{Z}) and neutron number (\mathcal{N}), also described as Coherent Elastic Neutrino-Nucleus Scattering (CE ν NS), serves as a crucial channel for testing the Standard Model (SM) of electroweak theory, especially in low energy regime.

A. Coherent Elastic Neutrino-Nucleus Scattering (CE ν NS)

CE ν NS, which involves neutral-current (NC) interactions between neutrinos and quarks within an atomic nucleus, is a tree-level process described within the SM. In this process, neutrinos interact coherently with a nucleus,

whether a proton or neutron, through neutral boson exchange at low energies. Coherent means that neutrinos can reach the inner structure of the nucleus without breaking it, i.e, the interaction occurs with the nucleus as a whole. The wavelength of the process is therefore larger than the nuclear radius, resulting in a momentum exchange on the scale of a few hundreds MeV. This implies that the complexity of the strong interaction can be encapsulated in a nuclear form factor. The process gives the largest cross-section compared to other neutrino interactions so far. The cross-section depends on the number of nucleons participated in the process. Particularly, since the weak mixing angle influences and limits the contribution from proton interactions, the observed cross-section is enhanced by the square of the neutron number. However, detecting this process is challenging due to the nuclear recoil energy being confined to the low keV scale. This criterion is necessary to ensure that the nucleus interacts with neutrino coherently. This challenging objective was finally accomplished with the advancement of accelerator neutrino technology in 2017 by the COHERENT Collaboration [4, 5], a few decades after its initial formulation [2].

Since the first detection of CE ν NS, numerous efforts have been made to better understand the phenomena. The COHERENT Collaboration updated their experiment using liquid Argon (LAr) [6]. They also announced the first detection of CE ν NS with pPC Ge detector, reinforcing the importance of Ge detectors in precision studies of low-energy neutrino interactions [7] and plan to further upgrade their experimental facilities by adapting

* Corresponding Author: karadags@itu.edu.tr

† Corresponding Author: muhammed.deniz@deu.edu.tr

liquid Xenon detector as a target. The CENNS team at Fermilab also aims to detect the $\text{CE}\nu\text{NS}$ process using the Booster Neutrino Beam at the facility [8]. Furthermore, reactor neutrino experiments are also contributing to the detection of the process in order to achieve lower nuclear threshold energy. The CONUS Collaboration provided strong limits [9] with Ge detectors at the Brokdorf Nuclear Power Plant in Germany. The follow-up CONUS+ project recently reported preliminary results [10] on a positive observation of $\text{CE}\nu\text{NS}$ at a significance of 3.7σ at the Leibstadt nuclear power plant (KKL) in Switzerland, marking a significant step in reactor neutrino $\text{CE}\nu\text{NS}$ searches. Alongside CONUS, other reactor-based efforts include TEXONO [11], which uses a Ge detector located at the Kuo-Sheng Nuclear Power Plant in Taiwan; CONNIE [12], with a CCD detector array at the Angra Power Plant in Rio de Janeiro, Brazil; RICOCHET [13] with both Ge-based and metallic Zn-based smaller detector at the Chooz Nuclear Power Plant in France; νGeN [14] with high purity Ge detector at the Kalinin Nuclear Power Plant in Russian; Dresden-II reactor experiment [15] with p-type point contact Ge detector in USA, MINER [16] at the Nuclear Science Center at Texas in USA.

Nuclear power plant experiments have high potential for observing the $\text{CE}\nu\text{NS}$ process, as they meet the coherency criteria ($> 95\%$) due to their high rate of low-energy neutrino flux [17]. Dark matter (DM) experiments, such as XENON-nT [18], DARWIN [19], LZ [20], and PandaX-4T [21], are also influenced by this channel, as $\text{CE}\nu\text{NS}$ plays a crucial role in the neutrino-floor phenomenon, providing an unavoidable background for DM experiments. Recently, the PandaX-4T [22] and XENONnT [23] experiments have reported the first measurements of nuclear recoils from solar ^8B neutrinos via $\text{CE}\nu\text{NS}$ with the corresponding statistical significance of 2.64σ and 2.73σ , respectively, representing the first experimental step towards the neutrino fog.

B. Non-Standard Interactions in $\text{CE}\nu\text{NS}$

The $\text{CE}\nu\text{NS}$ process opens up numerous opportunities to expand our understanding of physics. For example, it allows the investigation of neutrino and nuclear properties, such as study of the neutrino magnetic moment [24, 25]. Recent research has also explored potential explanations of sterile neutrinos [26]. Additionally, nuclear properties may be examined through this process [27]. $\text{CE}\nu\text{NS}$ plays an important role in astrophysical processes [2, 28] and has been proposed for detecting supernova neutrinos [29], providing a compact and transportable neutrino detector for real-time monitoring nuclear reactors [30], and studying neutron density distributions [31]. Moreover, the potential appearance of new fermions linked to neutrino mass and their role in explaining DM has been recently investigated [32]. The study of weakly interacting massive particle (WIMP) [33, 34]

as a candidate of DM is also related to $\text{CE}\nu\text{NS}$, as both share a similar nuclear recoil energy range in the few keV scale. ν -nucleus events from solar and atmospheric neutrinos represent an irreducible background [35, 36] for future DM direct detection experiments [37]. Additionally, measuring of the ν -nucleus scattering cross-section serves as a sensitive probe for new physics [38–40], potentially enabling the detection of new light bosons [41], which is crucial for advancing our understanding of novel interactions in nature.

Probing NSI with neutrino-nucleus scattering has been a subject of intense interest in recent years [40–47]. These studies have investigated various NSI scenarios, such as those based on simplified models focusing on light mediators [48–57], model-independent approaches effective in the high mediator mass regime [48, 58–62], and exotic neutral current interactions [63–65], along with experimental observables and implications for neutrino flavor physics [45, 66, 67] and astrophysical processes [68–70]. While significant progress has been made in probing NSI, most analyses remain limited to specific interaction types [53, 55, 58, 59] or single experimental environments [48–51], often concentrating on specific NSI scenarios. Comprehensive studies that simultaneously address all five interaction types are still missing. In addition, the studies of all possible NSI scenarios with both SNS and reactor neutrinos [43, 54, 71] offer complementary sensitivities, and are essential for achieving a deeper and more complete understanding of neutrino interactions.

C. Scope and Structure of This Work

In this paper, we provide a comprehensive analysis that bridges this gap by examining all five interaction types within both simplified model and model-independent frameworks. Our comparative results incorporate data from accelerator neutrino experiments (COHERENT), and reactor neutrino experiments (TEXONO). We explore a simplified model as an alternative approach to investigating physics beyond the SM (BSM). We consider generalized neutrino interactions (GNI) as well as the possibility of light mediators from simplified model, which includes all possible Lorentz-invariant interactions of vector (V), axialvector (A), scalar (S), pseudoscalar (P), and tensor (T) type. Each is assumed to involve light mediators that couple to neutrinos and the quark constituents of the nucleus. Notably, recent studies have employed an effective neutrino-quark approximation that includes these interaction types [63], and connections between this effective approximation and NSI have also been examined [72].

Our focused simplified model provides an alternative framework in particle physics to bridge theoretical prediction with experimental measurements. The experimental parameters considered in this model are limited to cross-sections, new particle masses, and couplings. It is important to emphasize that, unlike comprehensive

BSM extensions involving numerous particles and decay chains, this model does not fully represent the complexities of actual physics [73]. Nevertheless, explanatory models remain valuable for consideration, including those that can be embedded within potential SM extensions, either dependently or independently.

In this work, in particular, we present the first NSI analysis based on TEXONO experiments, using both nPC–Ge data from 2016 and recently released pPC–Ge data from 2024. We aimed at providing a complementary perspective by analysing COHERENT and TEXONO data, enabling a direct comparison of their constraints on NSI parameters. COHERENT probing accelerator-based neutrino interactions with multiple flavors at higher energies, while TEXONO with electron antineutrinos at lower energies. In this work, we cover a broader range of all possible interaction types in both simplified model and model-independent approach, as well as exotic neutral current interactions since previous studies focused on only limited set of interactions, such as vector and/or scalar type interactions in simplified model or vector type interaction in model-independent NSI.

In the following sections, we first provide a brief discussion of the theoretical formulation of CE ν NS, covering differential cross-sections and the effect of the form factor in Section II. In Subsection II A, we delve into GNI derived from simplified model. The formalism and structure of model-independent NSI of neutrinos are given in Subsection II B. Observation of CE ν NS through analysis of the COHERENT and TEXONO Experiments along with the calculations of expected event rates based on both the SM and BSM NSI theories are discussed in Section III. Our analysis methods and recent results are introduced in Section IV, starting with the relevant Lagrangian for the new interactions considered in the model and employing χ^2 -analysis methods. This section also presents our findings, including new constraints on coupling and mass parameter spaces, as well as on four-Fermi point-like interactions of ε -space, along with discussions of potential implications. Finally, we summarize and conclude our work in Section V.

We note that Ref.[10] have triggered numerous recent work [43, 46, 47, 71] on the NSI constraints based on the new yet preliminary data. We do not include these results in the discussions of this work.

II. FORMALISM

The scattering amplitude for the CE ν NS process, as shown in Fig. 1, can be expressed as ($q^2 \ll m_Z^2$)

$$\begin{aligned} \mathcal{M} &= \frac{G_F}{\sqrt{2}} \bar{\nu}(p_3) g_L^\nu \gamma^\mu (1 - \gamma^5) \nu(p_1) \\ &\quad \times \bar{N}(p_4) \gamma_\mu (Q_{\text{SM}_V} - \gamma^5 Q_{\text{SM}_A}) N(p_2), \end{aligned} \quad (2.1)$$

where G_F is the Fermi constant. We have used $G_F/\sqrt{2} = g_W^2/8m_W^2$ and $m_W = m_Z \cos \theta_W$, where g_W

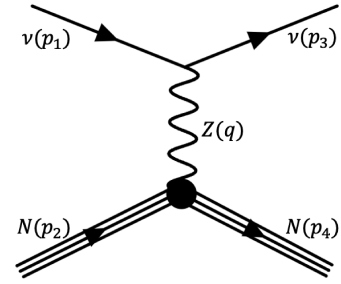


FIG. 1. Feynman diagram for CE ν NS process.

and $m_W(m_Z)$ are the weak coupling constant and W(Z) boson mass, respectively. The SM differential cross-section, incorporating both vector and axialvector weak charge components can be written as:

$$\begin{aligned} \left[\frac{d\sigma}{dT_N} \right]_{\text{SM}} &= \frac{G_F^2 m_N}{4\pi} \left(Q_{\text{SM}_V}^2 \mathcal{K}_V + Q_{\text{SM}_A}^2 \mathcal{K}_A \right. \\ &\quad \left. + 2Q_{\text{SM}_V} Q_{\text{SM}_A} \mathcal{K}_{VA} \right), \end{aligned} \quad (2.2)$$

where the kinetic terms of vector, axialvector and their mixing \mathcal{K}_V , \mathcal{K}_A and \mathcal{K}_{VA} can be described respectively as

$$\begin{aligned} \mathcal{K}_V &= 1 - \frac{m_N T_N}{2E_\nu^2} + \frac{T_N^2}{2E_\nu^2} - \frac{T_N}{E_\nu} \\ \mathcal{K}_A &= 1 + \frac{m_N T_N}{2E_\nu^2} + \frac{T_N^2}{2E_\nu^2} - \frac{T_N}{E_\nu} \\ \mathcal{K}_{VA} &= \frac{T_N^2}{2E_\nu^2} - \frac{T_N}{E_\nu} \end{aligned} \quad (2.3)$$

The axial and vector part of the weak charge, Q_{SM_A} and Q_{SM_V} can be written respectively as

$$\begin{aligned} Q_{\text{SM}_A} &= [S_n(\Delta_u^n - \Delta_d^n - \Delta_s^n) \\ &\quad + S_p(\Delta_u^p - \Delta_d^p - \Delta_s^p)] F(q^2), \\ Q_{\text{SM}_V} &= g_p^V \mathcal{Z} F_{\mathcal{Z}}(q^2) + g_n^V \mathcal{N} F_{\mathcal{N}}(q^2) \\ &= [\mathcal{Z}(1 - 4\sin^2 \theta_W) - \mathcal{N}] F(q^2). \end{aligned} \quad (2.4)$$

Here, $g_n^V = -1$ and $g_p^V = 1 - 4\sin^2 \theta_W$, where \mathcal{Z} and \mathcal{N} represent the proton and neutron numbers, respectively. $\sin^2 \theta_W$ is the weak mixing angle with a value of 0.23867 [1] at $q^2 \simeq 0$ [74]. The coefficients in the axial part are $\Delta_u^p = \Delta_d^n = 0.842$, $\Delta_d^p = \Delta_u^n = -0.427$ and $\Delta_s^p = \Delta_s^n = -0.085$ [75]. The spin expectation values, S_n and S_p , describe how much the neutrons and protons, respectively, within a nucleus contribute to the total nuclear spin. These dimensionless quantities are derived from theoretical nuclear structure model calculations and vary across different isotopes of a nucleus [76]. The axialvector contribution to the cross-section vanishes for nuclei with even number of protons and neutrons, which have spin-zero ground states. Moreover, in general the axial part can be neglected due to its small contribution

to the cross-section so the cross-section given in Eq. (2.2) simplifies considerably. In our analysis we adopt the following values for S_n and S_p based on simple shell model calculations presented in Ref. [77]:

- ^{133}Cs : $S_n = 0.001$ and $S_p = -0.343$,
- ^{127}I : $S_n = 0.031$ and $S_p = 0.346$,
- ^{23}Na : $S_n = 0.024$ and $S_p = 0.224$,
- ^{73}Ge : $S_n = 0.439$ and $S_p = 0.032$.

For ^{40}Ar , and most common isotopes of Ge (except ^{73}Ge), which have even numbers of both protons and neutrons, we have $S_n = S_p = 0$, resulting in no contribution to the total nuclear spin. The cross-section in Eq. (2.2) is enhanced by \mathcal{N}^2 due to the multiplication factor of g_p^V , making the contribution from the \mathcal{Z} boson relatively small. Despite the smallness of this factor, it remains important because it includes the weak mixing angle, $\sin^2 \theta_W$.

Nuclear physics effects in CE ν NS are incorporated via the weak nuclear form factors for neutrons, $F_{\mathcal{N}}$, and for protons, $F_{\mathcal{Z}}$, included in Eq. (2.4). In this work, these are assumed to be equal such that $F_{\mathcal{N}}(q^2) = F_{\mathcal{Z}}(q^2) = F(q^2)$. The three-momentum transfer ($q \equiv |\vec{q}|$) in terms of the measurable nuclear recoil energy of the target is given by $q^2 = 2m_N T + T^2 \simeq 2m_N T$. On the theoretical side, the ν -nucleus elastic scattering cross-section depends on the nuclear matrix element models and the nuclear structure details, which can be introduced through the nuclear form factors for protons and neutrons. Since there is no exact definition for the nuclear form factors, there are different methods to estimate them. In this study, we consider the Helm parametrization for the form factor, given as [78]

$$F_{\text{Helm}}(q^2) = 3 \frac{j_1(qR)}{qR} e^{-\frac{1}{2}q^2 s^2}. \quad (2.5)$$

Here, $j_1(x) = \sin x/x^2 - \cos x/x$ is the first order Spherical Bessel function. Nuclear radius is given by $R = \sqrt{c^2 - 5s^2}$, with the nuclear parameters $c = 1.2\mathcal{A}^{1/3}$ fm, $s = 0.5$ fm [79].

We present the Helm form factor for three different nuclei in Fig. 2. The chosen nuclei correspond to the detector materials used as targets in experiments such as COHERENT, TEXONO, CONUS, and others. As the recoil energy increases, the form factor reduces the observed quantity, thereby violating the coherency criteria. Further advancements in detecting this process will require detectors equipped with low-energy sensitive technology.

A. New Light Mediators from Simplified Model

To parametrise new physics at a very low scale, the light mediator models are constructed to include only

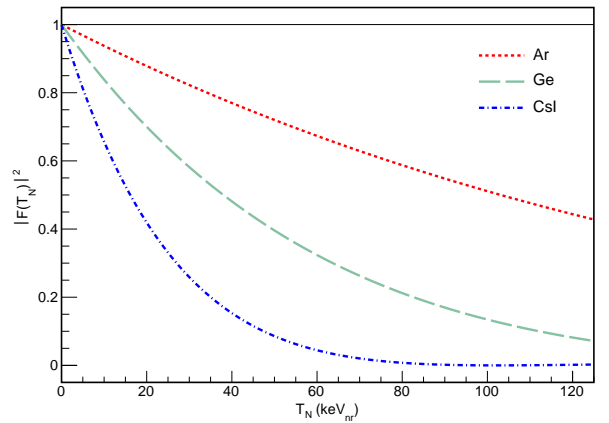


FIG. 2. Helm parameterization for Ar, Ge, and CsI as a function of T_N (keV_{nr}) is shown, with the case of full coherency, i.e., $F(T_N) \approx 1$, also included.

a few new particles and interactions in general vector, axial-vector, scalar, pseudoscalar and tensor form [42, 80]. These are so-called simplified models that have been intensively studied, e.g., in the dark matter searches at the LHC [81]. For measurements of neutrino-electron scattering or neutrino-nucleus scattering, such models are of interest because the mediators can have a pronounced effect on the recorded recoil spectra, most notably for mediator masses smaller than the maximum momentum transfer. The Lagrangians responsible for these interactions are

$$\begin{aligned} \mathcal{L}_V &\supset [g_{V\nu}\bar{\nu}_L\gamma^\mu\nu_L + g_{Vq}\bar{q}\gamma^\mu q]V_\mu, \\ \mathcal{L}_A &\supset [g_{A\nu}\bar{\nu}_L\gamma^\mu\nu_L - g_{Aq}\bar{q}\gamma^\mu\gamma^5 q]A_\mu, \\ \mathcal{L}_S &\supset [(g_{S\nu}\bar{\nu}_R\nu_L + h.c.) + g_{Sq}\bar{q}q]S, \\ \mathcal{L}_P &\supset [(g_{P\nu}\bar{\nu}_R\nu_L + h.c.) - ig_{Pq}\bar{q}\gamma^5 q]P, \\ \mathcal{L}_T &\supset [g_{T\nu}\bar{\nu}_R\sigma^{\mu\nu}\nu_L - g_{Tq}\bar{q}\sigma^{\mu\nu}q]T_{\mu\nu}, \end{aligned} \quad (2.6)$$

where $\sigma_{\mu\nu} = \frac{i}{2}[\gamma_\mu, \gamma_\nu] = \frac{i}{2}(\gamma_\mu\gamma_\nu - \gamma_\nu\gamma_\mu)$. With these Lagrangians, we can match the new mediator interactions from the quark level to the nuclear scale. We find the following for each interaction type:

$$\mathcal{L}_{XN} = g_{XN}\bar{N}NX F_X(T_N), \quad (2.7)$$

where $X = V, A, S, P, T$ and the coupling of the new mediators with nucleus are

$$\begin{aligned}
g_{VN} &= \mathcal{Z} \sum_q Q_q^p g_{Vq} + \mathcal{N} \sum_q Q_q^n g_{Vq}, \\
g_{AN} &= \mathcal{Z} \sum_q g_{Aq} S_p \Delta_q^p + \mathcal{N} \sum_q g_{Aq} S_n \Delta_q^n, \\
g_{SN} &= \mathcal{Z} \sum_q g_{Sq} \frac{m_p}{m_q} f_{Tq}^p + \mathcal{N} \sum_q g_{Sq} \frac{m_n}{m_q} f_{Tq}^n, \\
g_{PN} &= \mathcal{Z} \sum_q g_{Pq} \frac{m_p}{m_q} h_q^p + \mathcal{N} \sum_q g_{Pq} \frac{m_n}{m_q} h_q^n, \\
g_{TN} &= \mathcal{Z} \sum_q g_{Tq} \delta_q^p + \mathcal{N} \sum_q g_{Tq} \delta_q^n. \tag{2.8}
\end{aligned}$$

The parameters in the above relations are listed in Table I. The appearance of new interactions in the CE ν NS process is illustrated in Fig. 3.

TABLE I. Values of the simplified parameters.

Parameter	Value	Reference
$f_{T_u}^p$	0.0153	[75]
$f_{T_u}^n$	0.011	
$f_{T_d}^p$	0.0191	
$f_{T_d}^n$	0.0273	
$h_u^p = h_u^n$	0.825	[83]
$h_d^p = h_d^n$	0.375	
$Q_u^p = Q_d^n$	2	[53]
$Q_u^n = Q_d^p$	1	
$\delta_u^p = \delta_d^n$	0.84	[75]
$\delta_u^n = \delta_d^p$	-0.23	

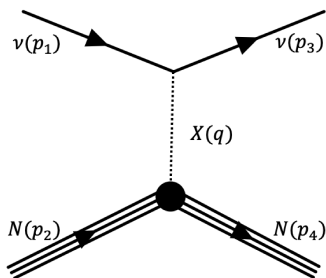


FIG. 3. Representative Feynman diagram for CE ν NS process with new mediator X.

It is worth noting that values for parameters involving strange quarks can be found in the literature; however, we have observed that their impact on our calculations for the NSI of CE ν NS is negligible. Therefore, we only consider the first lepton family quarks, namely the up and down quarks. We emphasize that the pseudoscalar interaction with the nucleus was considered negligible in previous works [80, 82], whereas in this study, we present the results from the lattice calculation [83]. The form factor in each case is assumed to be the same as the Helm parametrization in Eq. (2.5).

Concerning all of these, we obtain the differential cross-sections for the case of:

(i) Vector Interaction,

$$\begin{aligned}
\left[\frac{d\sigma}{dT_N} \right]_{\text{SM}+V} &= \frac{G_F^2 m_N}{4\pi} \left(Q_{\text{SM}V+V}^2 \mathcal{K}_V + Q_{\text{SM}A}^2 \mathcal{K}_A \right. \\
&\quad \left. + 2Q_{\text{SM}A} Q_{\text{SM}V+V} \mathcal{K}_{VA} \right), \tag{2.9}
\end{aligned}$$

here $Q_{\text{SM}V+V}$ is,

$$Q_{\text{SM}V+V} = Q_{\text{SM}V} + \frac{\sqrt{2}Q_V}{m_V^2 + 2m_N T_N}.$$

Vector differential cross-section without interference can be written as

$$\left[\frac{d\sigma}{dT_N} \right]_V = \frac{G_F^2 m_N}{4\pi} \frac{2Q_V^2}{(m_V^2 + 2m_N T_N)^2} \mathcal{K}_V. \tag{2.10}$$

The interference term of the differential cross-section can be written as

$$\begin{aligned}
\left[\frac{d\sigma}{dT_N} \right]_{V\text{INT}} &= \frac{G_F^2 m_N}{4\pi} \frac{2\sqrt{2}Q_V}{m_V^2 + 2m_N T_N} \\
&\quad \times \left(Q_{\text{SM}A} \mathcal{K}_{VA} + Q_{\text{SM}V} \mathcal{K}_V \right). \tag{2.11}
\end{aligned}$$

(ii) Axialvector Interaction,

$$\begin{aligned}
\left[\frac{d\sigma}{dT_N} \right]_{\text{SM}+A} &= \frac{G_F^2 m_N}{4\pi} \left(Q_{\text{SM}V}^2 \mathcal{K}_V + Q_{\text{SM}A+A}^2 \mathcal{K}_A \right. \\
&\quad \left. + 2Q_{\text{SM}V} Q_{\text{SM}A+A} \mathcal{K}_{VA} \right), \tag{2.12}
\end{aligned}$$

here $Q_{\text{SM}A+A}$ is,

$$Q_{\text{SM}A+A} = Q_{\text{SM}A} + \frac{\sqrt{2}Q_A}{m_A^2 + 2m_N T_N}.$$

Axial differential cross-section without interference can be written as

$$\left[\frac{d\sigma}{dT_N} \right]_A = \frac{G_F^2 m_N}{4\pi} \frac{2Q_A^2}{(m_A^2 + 2m_N T_N)^2} \mathcal{K}_A. \tag{2.13}$$

The interference term with axial differential cross-section can be written as

$$\begin{aligned}
\left[\frac{d\sigma}{dT_N} \right]_{A\text{INT}} &= \frac{G_F^2 m_N}{4\pi} \frac{2\sqrt{2}Q_A}{m_A^2 + 2m_N T_N} \\
&\quad \times \left(Q_{\text{SM}A} \mathcal{K}_A + Q_{\text{SM}V} \mathcal{K}_{VA} \right), \tag{2.14}
\end{aligned}$$

(iii) Scalar Interaction,

$$\left[\frac{d\sigma}{dT_N} \right]_S = \frac{G_F^2 m_N}{4\pi} \frac{Q_S^2}{(m_S^2 + 2m_N T_N)^2} \mathcal{K}_S, \tag{2.15}$$

where \mathcal{K}_S can be defined as

$$\mathcal{K}_S = \frac{m_N T_N}{E_\nu^2} + \frac{T_N^2}{2E_\nu^2} \tag{2.16}$$

(iv) Pseudoscalar Interaction,

$$\left[\frac{d\sigma}{dT_N} \right]_P = \frac{G_F^2 m_N}{4\pi} \frac{Q_P^2}{(m_P^2 + 2m_N T_N)^2} \mathcal{K}_P, \quad (2.17)$$

where \mathcal{K}_P can be defined as

$$\mathcal{K}_P = \frac{T_N^2}{2E_\nu^2} \quad (2.18)$$

(v) Tensor Interaction,

$$\left[\frac{d\sigma}{dT_N} \right]_T = \frac{G_F^2 m_N}{4\pi} \frac{16Q_T^2}{(m_T^2 + 2m_N T_N)^2} \mathcal{K}_T, \quad (2.19)$$

where \mathcal{K}_T can be defined as

$$\mathcal{K}_T = 1 - \frac{m_N T_N}{4E_\nu^2} + \frac{T_N^2}{4E_\nu^2} - \frac{T_N}{E_\nu}. \quad (2.20)$$

In all these equations the new charges Q_X can be defined as

$$Q_X = \frac{g_{X\nu} g_{XN} F(q^2)}{G_F}, \quad (2.21)$$

where X stands for the different interaction channels of V, A, S, P, and T.

B. Model Independent Non-Standard Interactions of Neutrino

One of the most extensively studied models in the search of new physics BSM is the NSI of neutrinos [84]. NSI interactions of neutrinos, in a model-independent approach, can be described as a four-Fermi point-like interaction, as shown in Fig. 4. This model introduces a new type of contact interactions between neutrinos and matter distinct from the SM theory [45]. In general, NSI can induce a neutral current (NC) and charge current (CC) processes, each implying the presence of a new mediator with heavier mass [85] or in the same order as the EW theory [86]. For CE ν NS, only the NC case is relevant. Neutrinos with NSI influence quarks inside a nucleus, interacting either as a non-universal flavor-conserving (FC) or flavor-violating (FV) process. In general, the Lagrangians given in terms of model-independent coupling constant in Eq. (2.6) can be modified to describe model-independent NSI by replacing coupling g_X with ε using the relation provided in Eq. (2.24). Specifically, the V-A type for model-independent NSI can be formulated as

$$-\mathcal{L}_{NSI}^{eff} = \varepsilon_{\alpha\beta}^{fP} 2\sqrt{2}G_F (\bar{\nu}_\alpha \gamma_\mu L \nu_\beta) (\bar{f}' \gamma^\mu P f), \quad (2.22)$$

with $\varepsilon_{\alpha\beta}^{fP}$ is the coupling that describes the strength of the NSI, f is a first generation SM fermion (e, u, or d) in which $f = f'$ refers to NC NSI, whereas CC NSI are obtained for $f' \neq f$, P denotes the chiral projector

$L, R = (1 \pm \gamma^5)/2$, α and β denote the neutrino flavor (e, μ , or τ).

The relevant Lagrangian for CE ν NS NC process can be written as

$$-\mathcal{L}_{NSI}^{eff} = \frac{G_F}{\sqrt{2}} [\bar{\nu}_\alpha \gamma_\mu (1 - \gamma^5) \nu_\beta] [\bar{f} \gamma^\mu (\varepsilon_{\alpha\beta}^{fV} - \varepsilon_{\alpha\beta}^{fA} \gamma^5) f], \quad (2.23)$$

The NSI coupling $\varepsilon_{\alpha\beta}^{fX}$ can be express as

$$\varepsilon_{\alpha\beta}^{fX} \simeq \frac{\sqrt{2}}{G_F} \frac{g_{X\nu} g_{XN}}{M_X^2}, \quad (2.24)$$

where g_X and M_X stand for the coupling constant and mass of the mediator, respectively.

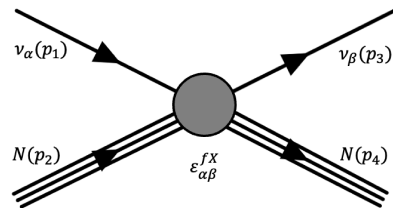


FIG. 4. The Feynman diagram for four-Fermi point-like interaction.

Hence, the differential cross-section of NSI can be written as:

(i) for the vector case

$$\left[\frac{d\sigma}{dT_N} \right]_V^{NSI} = \frac{G_F^2 m_N}{\pi} |F(q^2)|^2 \left[\varepsilon_{\alpha\beta}^{uV} (\mathcal{N} + 2\mathcal{Z}) + \varepsilon_{\alpha\beta}^{dV} (2\mathcal{N} + \mathcal{Z}) \right]^2 \mathcal{K}_V, \quad (2.25)$$

where $\alpha = \beta = e, \mu, \tau$ is corresponding to FC type of interaction and $\alpha \neq \beta = e, \mu, \tau$ is corresponding to FV case.

The interference term for the FC case only can be written as

$$\left[\frac{d\sigma}{dT_N} \right]_{V_{INT}}^{FC} = \frac{G_F^2 m_N}{\pi} |F(q^2)|^2 \times \left[\varepsilon_{\alpha\beta}^{uV} (\mathcal{N} + 2\mathcal{Z}) + \varepsilon_{\alpha\beta}^{dV} (2\mathcal{N} + \mathcal{Z}) \right] \times \left[(1 - 4 \sin^2 \theta_W) \mathcal{Z} - \mathcal{N} \right] \mathcal{K}_V, \quad (2.26)$$

(ii) for the axial case;

$$\left[\frac{d\sigma}{dT_N} \right]_A^{NSI} = \frac{G_F^2 m_N}{\pi} |F(q^2)|^2 \left[\varepsilon_{\alpha\beta}^{uA} (\mathcal{N} S_n \Delta_u^n + \mathcal{Z} S_p \Delta_u^p) + \varepsilon_{\alpha\beta}^{dA} (\mathcal{N} S_n \Delta_d^n + \mathcal{Z} S_p \Delta_d^p) \right]^2 \mathcal{K}_A, \quad (2.27)$$

(iii) for the scalar case;

$$\begin{aligned} \left[\frac{d\sigma}{dT_N} \right]_S^{NSI} &= \frac{G_F^2 m_N}{2\pi} |F(q^2)|^2 \\ &\times \left[\varepsilon_{\alpha\beta}^{uS} (\mathcal{N} \frac{m_n}{m_u} f_{Tu}^n + \mathcal{Z} \frac{m_p}{m_u} f_{Tu}^p) \right. \\ &\left. + \varepsilon_{\alpha\beta}^{dS} (\mathcal{N} \frac{m_n}{m_d} f_{Td}^n + \mathcal{Z} \frac{m_p}{m_d} f_{Td}^p) \right]^2 \mathcal{K}_S, \end{aligned} \quad (2.28)$$

(iv) for the pseudoscalar case;

$$\begin{aligned} \left[\frac{d\sigma}{dT_N} \right]_P^{NSI} &= \frac{G_F^2 m_N}{2\pi} |F(q^2)|^2 \\ &\times \left[\varepsilon_{\alpha\beta}^{uP} (\mathcal{N} \frac{m_n}{m_u} h_u^n + \mathcal{Z} \frac{m_p}{m_u} h_u^p) \right. \\ &\left. + \varepsilon_{\alpha\beta}^{dP} (\mathcal{N} \frac{m_n}{m_d} h_d^n + \mathcal{Z} \frac{m_p}{m_d} h_d^p) \right]^2 \mathcal{K}_P, \end{aligned} \quad (2.29)$$

(v) for the tensor case;

$$\begin{aligned} \left[\frac{d\sigma}{dT_N} \right]_T^{NSI} &= \frac{8G_F^2 m_N}{\pi} |F(q^2)|^2 \left[\varepsilon_{\alpha\beta}^{uT} (\mathcal{N} \delta_u^n + \mathcal{Z} \delta_u^p) \right. \\ &\left. + \varepsilon_{\alpha\beta}^{dT} (\mathcal{N} \delta_d^n + \mathcal{Z} \delta_d^p) \right]^2 \mathcal{K}_T. \end{aligned} \quad (2.30)$$

C. Exotic Neutral Currents In Coherent ν -N Scattering

Apart from the model-independent NSI in epsilon-space $\varepsilon_{\alpha\beta}^{qX}$ additional, more ‘‘exotic’’ new interactions could be present. Five possible types of such ‘‘exotic’’ interactions can be introduced namely vector (V), axialvector (A), scalar (S), pseudoscalar (P), and tensor (T). The Lagrangian at the quark level for these interactions, considering all Lorentz-invariant interactions of neutrinos with first generation quarks, can be formulated as:

$$\mathcal{L} = \frac{G_F}{\sqrt{2}} \sum_X \bar{\nu} \Gamma^X \nu \left[\bar{q} \Gamma^X (C_X^q + i\gamma^5 D_X^q) q \right], \quad (2.31)$$

here again X represents for V, A, S, P, T and we only consider first generation of quarks, where q stands for u and d quarks, and Γ^X can be described as

$$\Gamma^X = \{ \gamma^\mu, \gamma^\mu \gamma^5, I, i\gamma^5, \sigma^{\mu\nu} \}, \quad (2.32)$$

for V, A, S, P, and T, respectively.

Analogous to Eq. (2.24), the coefficients C_X^q and D_X^q are expected to be of the order $(g_X^2/g^2)(m_W^2/m_X^2)$, where m_X represents the mass of the new exchange particles and g_X denotes their coupling constants. The coefficients C_X^q and D_X^q in Eq. (2.31) are dimensionless and, in principle, can be complex numbers. However for simplicity, we assume these parameters C_X^q and D_X^q to be real [44].

By analogy with Eqs. (2.7) and (2.8) the neutrino-nucleus (ν -N) effective Lagrangian, transitioning from the quark level to the nucleus scale, can be expressed as

$$\begin{aligned} \mathcal{L}_{\nu-N} \supset &\sum_{X=S,V,T} \bar{\nu} \Gamma^X \nu \left[\bar{N} C_X \Gamma^X N \right] \\ &+ \sum_{(X,Y)=(S,P),(V,A)} \bar{\nu} \Gamma^X \nu \left[\bar{N} i D_X \Gamma^Y N \right]. \end{aligned} \quad (2.33)$$

Here the expression for C_X and D_X can be derived from Eq. (2.8). It is worth noting that different notation for the couplings (g_{XN}) was used in Section II A.

Since the effective couplings for nuclear spin-dependent interactions are determined by the sum over spin-up and spin-down nucleons, axial and pseudoscalar currents are suppressed in heavy nuclei. Consequently, the most significant contributions are expected from scalar, vector and tensor quark currents. As such, we can constraint the quark currents can be considered as C_S^q , D_P^q , C_V^q , D_A^q , and C_T^q . The expression for D_P can be obtained from that of C_S by replacing C_S^q with D_P^q , while D_A can be derived from C_V by substituting C_V^q with D_A^q [63, 64].

$$\begin{aligned} \left[\frac{d\sigma}{dT_N} \right]_{EXO} &= \frac{G_F^2 m_N}{4\pi} |F(q^2)|^2 \mathcal{N}^2 \left[(\xi_V + \xi_{SM})^2 \mathcal{K}_V \right. \\ &\quad + \xi_A^2 \mathcal{K}_A - 2\xi_V \xi_A \mathcal{K}_{VA} + \xi_S^2 \mathcal{K}_S \\ &\quad \left. + \xi_T^2 \mathcal{K}_T - R \mathcal{K}_{VA} \right], \end{aligned} \quad (2.34)$$

where the new exotic couplings can be defined in terms of the coefficients C_X and D_X as

$$\begin{aligned} \xi_V^2 &= \frac{C_V^2 + D_A^2}{\mathcal{N}^2} \\ \xi_A^2 &= \frac{D_V^2 + C_A^2}{\mathcal{N}^2} \\ \xi_V \xi_A &= \frac{C_V D_V + C_A D_A}{\mathcal{N}^2} \\ \xi_S^2 &= \frac{C_S^2 + D_P^2}{\mathcal{N}^2} \\ \xi_T^2 &= 8 \frac{C_T^2 + D_T^2}{\mathcal{N}^2} \\ R &= 2 \frac{C_P C_T - C_S C_T + D_T D_P - D_T D_S}{\mathcal{N}^2}. \end{aligned} \quad (2.35)$$

While different notations exist in the literature to represent the SM contribution [63, 64], we adopt the convention used in Refs. [60, 65]. Specifically, $\xi_{SM} = [\mathcal{Z}(1 - 4\sin^2\theta_W) - \mathcal{N}]/\mathcal{N}$ is used to represent the SM contribution in Eq. (2.34). The first two lines of Eq. (2.34) encompass the vector interaction including the SM contribution, the axial-vector interaction, the scalar interaction, which involves interference with pseudoscalar terms. The last line includes the tensor interaction, while the R term accounts for the interference between the (pseudo-) scalar and tensor interactions.

III. EXPERIMENTAL DATA AND EVENT RATES

The expected number of event can be calculated from

$$R_X = N_{tar} \int_{T_{Nmin}}^{T_{Nmax}} dT_N \int_{E_{\nu min}}^{E_{\nu max}} dE_{\nu} \frac{d\Phi}{dE_{\nu}} \left[\frac{d\sigma}{dT_N} \right]_X, \quad (3.1)$$

where X represents different interaction channels such as the SM, NSI, etc., $d\Phi/dE_{\nu}$ is the neutrino spectra shown in Fig. 5, $d\sigma/dT_N$ is differential cross-section of the process, and N_{tar} is the total number of target nucleons.

A nuclear recoil threshold of $T_{Nmin} < 2E_{\nu}^2/m_N$ is required to detect neutrinos with energy E_{ν} . From kinematics, the maximum recoil energy is defined as $T_{Nmax} = 2E_{\nu}^2/(m_N + 2E_{\nu}) \simeq 2E_{\nu}^2/m_N$.

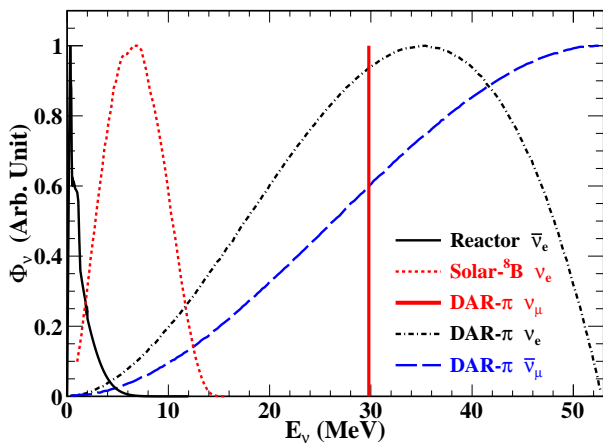


FIG. 5. Neutrino spectra (Φ_{ν}) for reactor $\bar{\nu}_e$, solar- 8B ν_e , and DAR- π ($\nu_{\mu}, \nu_e, \bar{\nu}_{\mu}$) neutrinos are adapted from Ref. [4, 89–92] and normalized to their respective maxima.

Scattering of neutrinos off nuclei provides an opportunity to test the SM and investigate new physics BSM with several promising experimental programs proposed. In particular, nuclear power reactors and stopped-pion neutrino facilities hold the potential to serve as optimal tool for studying of neutrino-nucleus scattering processes [11, 87, 88].

The TEXONO Collaboration is conducting an intense research program on low-energy neutrino physics (<10 MeV) at the Kuo-Sheng Nuclear Power Plant in Taiwan. The collaboration conducted an experiment in 2016 using a high-purity n-type point-contact germanium (nPC-Ge) detector cooled by liquid nitrogen and upgraded its facilities in 2024 with an advanced p-type point-contact germanium (pPC-Ge) detector. In the present study, 124.2(70.3) kg-days reactor ON(OFF) data collected at Kuo-Sheng Neutrino Laboratory (KSNL) with a threshold energy of 300 eV [93], and 242(357) kg-days reactor ON(OFF) data with an improved threshold energy of 200 eV [94] are analysed.

Nuclear reactors serve as experimental facilities, offering significantly larger fluxes of electron type antineutri-

nos ($\bar{\nu}_e$) compared to other neutrino sources. Stopped-pion facilities produce laboratory neutrinos generated from pion and muon decays at rest (DAR- π) in muon factories. These neutrinos are intermediate in energy, with a maximum energy of 52.8 MeV. To empirically confirm the SM theory or identify signs of new physics BSM, ν -nucleus scattering studies can be conducted using the realistic reactor $\bar{\nu}_e$ and DAR- π ($\nu_{\mu}, \nu_e, \bar{\nu}_{\mu}$) sources. Upcoming neutrino experiments with low-threshold detectors capable of detecting reactor $\bar{\nu}_e$ could provide for observing NSI effects, while DAR- π ($\nu_{\mu}, \nu_e, \bar{\nu}_{\mu}$) sources offer opportunities to measure cross-sections and explore new neutrino interactions in experiments with higher threshold detectors. In this context, COHERENT and TEXONO experiments provide complementary insights into CE ν NS by covering different energy ranges, neutrino sources, and detector technologies.

In order to predict the number of observable events in the detectors, it is essential to account for detector quenching, resolution, and detection efficiency functions. First, the nuclear recoil energy T_N (or E_{nr}) must be converted into the electron-equivalent energy E_{ee} using the quenching function, Q_F , such that

$$E_{ee} = Q_F(T_N) \times T_N. \quad (3.2)$$

Then the differential cross-section of $d\sigma/dT_N$ can be converted into $d\sigma/dE_{ee}$ by

$$\frac{d\sigma}{dE_{ee}} = \left(\frac{d\sigma}{dT_N} \right) \left(\frac{dT_N}{dE_{ee}} \right) \quad (3.3)$$

Subsequently, the predicted electron-equivalent energy E_{ee} must be smeared by energy resolution function in order to transform the calculated event rate into the observable event rate within specific energy bins. Finally, the predicted event rate must be processed through the detector efficiency function to align the predicted and observed rates, ensuring they are directly comparable.

For the COHERENT CsI(Na) detector, the Q_F is defined as

$$E_{ee} = aT_N + bT_N^2 + cT_N^3 + dT_N^4, \quad (3.4)$$

where the coefficients of a, b, c, and d are given in Ref. [5].

In the CsI(Na) detector, the light yield is specified as 13.35 photons/keV $_{ee}$. The energy resolution function is modelled using a gamma function expressed as

$$P(x) = \frac{[a(1+b)^{1+b}]}{\Gamma(1+b)} x^b e^{-a(1+b)x}, \quad (3.5)$$

where $a = 1/E_{ee}$ and $b = 0.71571E_{ee}$ are in photoelectrons (PE) unit.

The energy efficiency was determined by using data from ^{133}Ba calculations and is expressed as

$$Eff(E_{ee}) = \frac{a}{1 + e^{-b(E_{ee}-c)} + d}, \quad (3.6)$$

where the coefficients of a, b, c, and d are given in Ref. [5].

For LAr detector [6], the Q_F is given as

$$E_{ee} = 0.246 + 7.8 \times 10^{-4} T_N, \quad (3.7)$$

where T_N is in keV unit.

The energy resolution function, described as a Gaussian function, which was determined using ^{83m}Kr calibration data is expressed as

$$\sigma_E/E_{ee} = 0.58/\sqrt{E_{ee}}, \quad (3.8)$$

where E_{ee} is in keV unit. The detection efficiency is also given in Ref. [6].

The Q_F for the TEXONO HPGe detector is provided using the standard Lindhard Model, expressed as

$$Q_F = \frac{k g(\epsilon)}{1 + k g(\epsilon)}, \quad (3.9)$$

where $g(\epsilon)$ is from fitting by [95] with the function of

$$g(\epsilon) = 3\epsilon^{0.15} + 0.7\epsilon^{0.6} + \epsilon, \quad (3.10)$$

where $\epsilon = 11.5 Z^{-7/3} T_N$, with T_N in keV, and k is a measure of the electronic energy loss, which is given by the standard Lindhard Model as $k \approx 0.157$ for Ge [96], applicable to the TEXONO nPC-Ge detector. In its latest study with pPC-Ge detector, the TEXONO collaboration measured $k \approx 0.162$ [94].

Energy resolution function is described as a Gaussian energy resolution function given as

$$\sigma^2 = \sigma_o^2 + E_{ee}\eta F, \quad (3.11)$$

where σ_o , obtained by Root-Mean-Square (RMS) of test-pulsers, is $49 eV_{ee}$ for the nPC-Ge detector and $31.37 eV_{ee}$ for pPC-Ge detector, $\eta = 2.96 eV_{ee}$ is the average energy required for photons to create an electron-hole pair in Ge, and $F \approx 0.105$ is the Fano factor taken from Ref. [97].

IV. ANALYSIS AND RESULTS

A. Event Rate Predictions

In this section, we present our analysis results derived from TEXONO nPC-Ge(2016) and pPC-Ge(2024), COHERENT CsI and LAr data for each model under consideration.

To constrain the parameters, we adapt the analysis method based on the minimum χ^2 -method. The TEXONO and COHERENT updated data are analysed using a 1-bin analysis by minimizing

$$\chi^2 = \sum_i \left[\frac{R_{\text{expt}}(i) - R_{\text{SM}}(i) - R_X(i)}{\Delta(i)} \right]^2, \quad (4.1)$$

where R_{expt} is the measured event rate, and R_{SM} and R_X are the expected event rates for the SM and X (represents

NSI with $X = \text{V, A, S, P, T, etc}$), respectively; and Δ is the i^{th} bin statistical uncertainty published by the experiments.

Differential cross-sections as a function of recoil energy T_N for V, A, S, P, and T type NSI are shown in Fig. 6. These cross-sections are based on both the simplified model and the model-independent approach, calculated for specific mass and coupling parameters using data from the TEXONO pPC-Ge, and COHERENT CsI(Na) and LAr experiments. In Fig. 6, we present the predicted differential event rates for the SM CE ν NS process (solid-black) alongside possible new interactions considered in both the simplified model (left panel) and the model-independent NSI framework (right panel). The event rates are categorized by interaction type: V (dotted-light blue), V_{+INT} (dashed-dark blue), A (dash dotted-purple), A_{+INT} (long dashed-magenta), S (long dash dotted-red), P (dash double dotted-orange), and T (dash triple dotted-green). The SM differential event rates are calculated using Eq. (3.1), while the corresponding differential cross-sections are derived from Eq. (2.2). For the NSI differential cross-sections, the equations from Eq. (2.10) to Eq. (2.19) are employed for simplified model and the equations from Eq. (2.25) to Eq. (2.30) are used for the model-independent approach. In this analysis, we consider a mediator mass parameter of $m_X = 10$ MeV and coupling constants varying in the range $g_X = 0.1 - 7 \times 10^{-4}$ for each interaction type. The representative values chosen for the coupling constants are as follows:

(i) for COHERENT CsI(Na)

$$g_V = 3 \times 10^{-5}, g_A = 7 \times 10^{-4}, g_S = 3 \times 10^{-5}, \\ g_P = 3 \times 10^{-4}, g_T = 6 \times 10^{-5};$$

(ii) for COHERENT LAr,

$$g_V = 5 \times 10^{-5}, g_S = 3 \times 10^{-5}, g_P = 1 \times 10^{-4}, \\ g_T = 6 \times 10^{-5};$$

(iii) and for TEXONO pPC-Ge,

$$g_V = 4 \times 10^{-5}, g_A = 3 \times 10^{-4}, g_S = 1 \times 10^{-5}, \\ g_P = 2 \times 10^{-4}, g_T = 3 \times 10^{-5}.$$

We observe that when the recoil energy, T_N , is below around 10 keV for the COHERENT CsI(Na) experiment, below around 50 keV for the LAr experiment, and below around 1 keV for the TEXONO pPC-Ge experiment, the new interactions deviate significantly from the SM and also differ notable from each other. However, as the nuclear recoil energy increases, the new interactions tend to converge towards the SM prediction and, in some cases, overlap with them. This behavior can primarily be attributed to the dependence of the cross-sections on the $2m_N T_N$ term in the denominator. As the nuclear recoil energy decreases, this term becomes dominant, causing a rapid increase in the cross-sections of the new interactions. Therefore, the spectra of new interactions exhibit different tendencies from the SM in the low energy regime

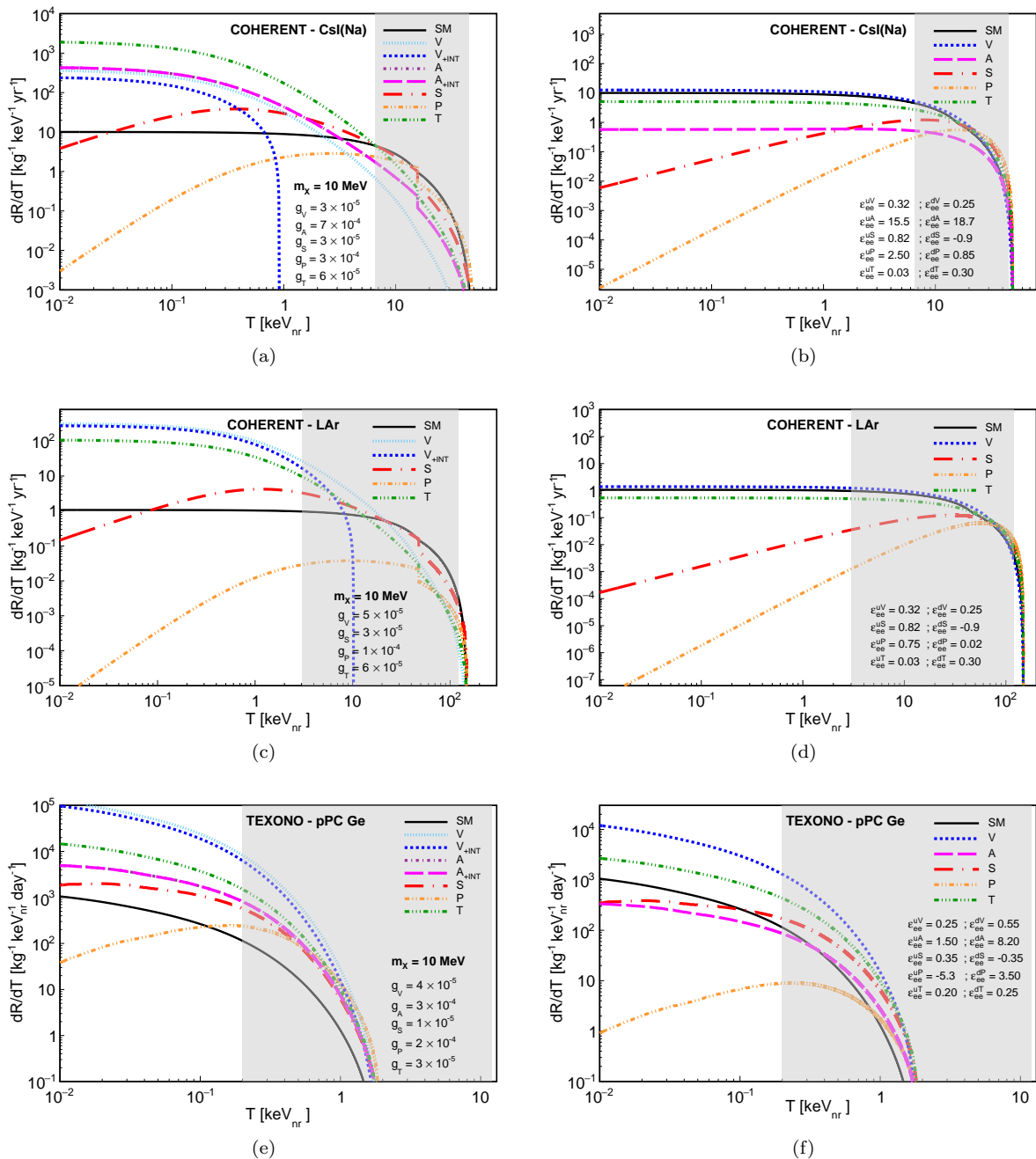


FIG. 6. Predicted differential cross-section as a function of the recoil energy T_N are shown for typical neutrino spectra corresponding to V, A, S, P, and T type NSI with specific mass and coupling parameters, (left panel) as well as ε_{ee}^{fX} (right panel). These predictions are presented for the following experiments: (a) and (b) COHERENT Csl(Na) [4, 5], (c) and (d) COHERENT LAr [6], (e) and (f) TEXONO pPC-Ge [94]. (The gray-shaded regions indicate the region-of-interest (ROI) for each experiment.)

and deviate more from the SM expectation as one moves towards the low recoil energy regime.

For model-independent NSI, we identify values near the best-fit points for all possible new interaction types in scenarios where two epsilon parameters are present simultaneously. As a reference, we present the $\varepsilon_{ee}^{uX} - \varepsilon_{ee}^{dX}$ case in Fig. 6 (right panel). The values adopted to

generate this reference plot are as follows:

(i) for COHERENT CsI(Na),

$$\begin{aligned} \varepsilon_{ee}^{uV} &= 0.32, \quad \varepsilon_{ee}^{dV} = 0.25, \quad \varepsilon_{ee}^{uA} = 15.5, \quad \varepsilon_{ee}^{dA} = 18.7, \\ \varepsilon_{ee}^{uS} &= 0.82, \quad \varepsilon_{ee}^{dS} = -0.90, \quad \varepsilon_{ee}^{uP} = 2.50, \quad \varepsilon_{ee}^{dP} = 0.85, \\ \varepsilon_{ee}^{uT} &= 0.03, \quad \varepsilon_{ee}^{dT} = 0.30; \end{aligned}$$

(ii) for COHERENT LAr,

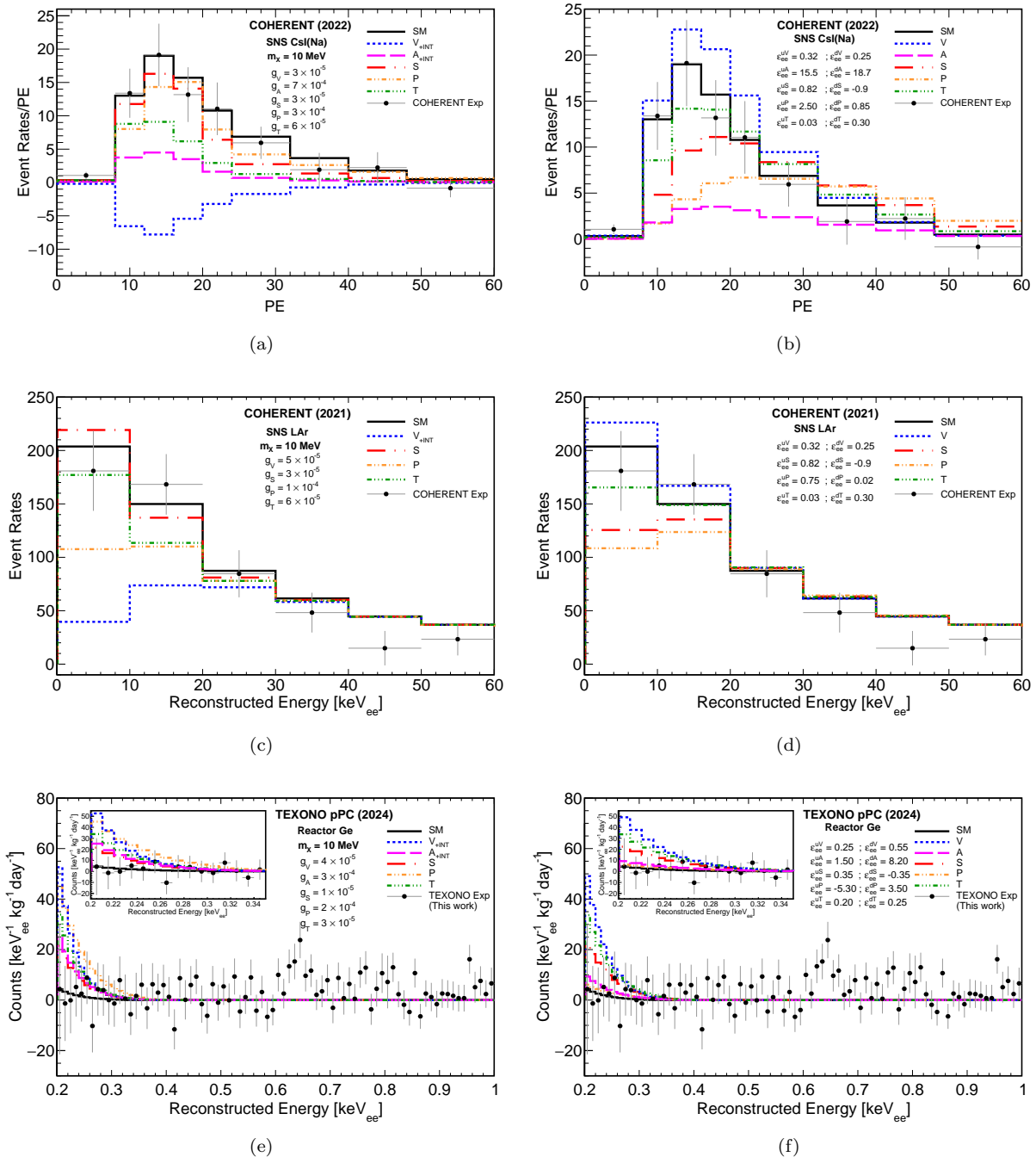


FIG. 7. Comparison of published experimental and expected event rates is shown for the COHERENT CsI(Na) [4, 5] (upper panel), COHERENT LAr [6] (middle panel), and TEXONO pPC-Ge [94] (bottom panel) experiments alongside the SM prediction calculations. These predictions incorporate quenching factors, response functions, and efficiencies provided by the COHERENT and TEXONO Collaborations. The dotted, dashed, dash-dotted, long-dashed, long-dash-dotted, dash-double-dotted, and dash-triple-dotted histograms represent the expected event rates for various NSI cases with arbitrary values for mass and coupling parameters (left panel), and ϵ_{ee}^{fX} values (right panel), for comparison.

$$\begin{aligned} \epsilon_{ee}^{uV} &= 0.32, \quad \epsilon_{ee}^{dV} = 0.25, \quad \epsilon_{ee}^{uS} = 0.82, \quad \epsilon_{ee}^{dS} = -0.90, \\ \epsilon_{ee}^{uP} &= 0.75, \quad \epsilon_{ee}^{dP} = 0.02, \quad \epsilon_{ee}^{uT} = 0.03, \quad \epsilon_{ee}^{dT} = 0.30; \end{aligned}$$

$$\begin{aligned} \epsilon_{ee}^{uS} &= 0.35, \quad \epsilon_{ee}^{dS} = -0.35, \quad \epsilon_{ee}^{uP} = -5.30, \quad \epsilon_{ee}^{dP} = 3.50, \\ \epsilon_{ee}^{uT} &= 0.20, \quad \epsilon_{ee}^{dT} = 0.25. \end{aligned}$$

(iii) and for TEXONO pPC-Ge,

$$\epsilon_{ee}^{uV} = 0.25, \quad \epsilon_{ee}^{dV} = 0.55, \quad \epsilon_{ee}^{uA} = 1.50, \quad \epsilon_{ee}^{dA} = 8.20,$$

We present expected number of events for the TEXONO and COHERENT experiments in Fig. 7. The upper

TABLE II. Summary of 90% CL upper limits for vector, axialvector, scalar, pseudoscalar, and tensor NSI measurements for the coupling constant parameter for the scenarios $m_X^2 \ll 2m_N T_N$ and $m_X^2 \gg 2m_N T_N$ derived from COHERENT CsI and LAr, and TEXONO nPC-Ge (2016) and pPC-Ge (2024) experiments data.

		$(m_X^2 \ll 2m_N T_N)$				$(m_X^2 \gg 2m_N T_N)$				
Fitting		TEXONO($\times 10^{-5}$)		COHERENT($\times 10^{-5}$)		Fitting	TEXONO($\times 10^{-6}$)		COHERENT($\times 10^{-6}$)	
Par		nPC-Ge	pPC-Ge	CsI(Na)	LAr	Par	nPC-Ge	pPC-Ge	CsI(Na)	LAr
g_V		< 5.54	< 2.57	< 2.22	< 4.37	g_V/m_V	< 4.25	< 2.18	< 1.76	< 1.40
g_A		< 49.6	< 20.7	< 66.6	–	g_A/m_A	< 36.3	< 17.0	< 11.45	–
g_S		< 1.70	< 0.72	< 2.03	< 2.66	g_S/m_S	< 1.24	< 0.59	< 0.33	< 0.62
g_P		< 26.2	< 11.8	< 19.5	< 18.3	g_P/m_P	< 18.9	< 9.40	< 2.82	< 3.21
g_T		< 4.69	< 1.93	< 5.05	< 4.07	g_T/m_T	< 3.45	< 1.59	< 0.87	< 1.17

panel illustrates data from the COHERENT CsI [5] experiment as a function of PE, shown by black dots. Similarly, the middle panel presents spectral data from the COHERENT LAr experiment [6], and the bottom panel corresponds to the TEXONO pPC-Ge experiment [94], both plotted against reconstructed energy (keV_{ee}), also represented by black dots. The SM event predictions are shown as solid black lines. To explore the effects of NSI on $\text{CE}\nu\text{NS}$, we also provide the estimated number of events in both the mass-coupling (left panel) and double-epsilon (right panel) parameter spaces. The parameter values are selected from the 90% C. L. (CL) range shown in Fig. 6.

B. Bounds from Simplified Model

Eq.s (2.10) - (2.19) indicate that the cross-section for all interaction types depends on the mass and coupling constant in the form $g_X^2/(m_X^2 + 2M_N T_N)$. Based on this dependence, the resulting limits exhibit distinct trends: in the low-mass regime ($m_X \lesssim 10$ MeV), the upper limits are determined solely by the coupling constant g_X , while in the high-mass regime ($m_X \gtrsim 10$ MeV), the limits scale with g_X/m_X (as shown in Figure 8). Taking this behavior into account, Table II provides a summary of the corresponding upper limits at 90% CL for the coupling constant parameters associated with vector, axialvector, scalar, pseudoscalar and tensor NSI within the simplified model for two distinct mass regimes, $m_X^2 \ll 2m_N T_N$ and $m_X^2 \gg 2m_N T_N$, across the TEXONO nPC-Ge and pPC-Ge, and COHERENT CsI(Na) and LAr experiments. The first section of Table II corresponds to the $m_X^2 \ll 2m_N T_N$ case, and lists the 90% CL upper limits for the coupling constants. The latter section focuses on the $m_X^2 \gg 2m_N T_N$ case, and showing the 90% CL upper limits for the slope of g_X/m_X . Table II highlights the varying sensitivity of each experiment and interaction type, with some coupling constants being more tightly constrained than others. Notably, the TEXONO pPC-Ge experiment imposes the most stringent limits on the scalar interaction, $g_S < 0.72 \times 10^{-5}$, while the CO-

HERENT CsI detector provides the tightest constraint on the vector interaction, $g_V < 2.22 \times 10^{-5}$.

Building on the results summarized in Table II, Figure 8 offers a detailed visualization of the 90% CL exclusion plots for all possible interaction types (V, A, S, P, and T) in the mass-coupling $m_X - g_X$ parameter space. These plots illustrate how the upper limits on the coupling constants evolve across different mediator masses, and for comparison, we also include the constraints from other $\text{CE}\nu\text{NS}$ experiments, such as CONUS [49], CONNIE [50], and Dresden-II [52], particularly for vector and scalar interactions. In Fig. 8a, we see that CONNIE provides the best upper limit for lower mediator masses in vectorial case, with COHERENT CsI and TEXONO pPC-Ge offering a slightly weaker limits, followed by Dresden-II, CONUS, COHERENT LAr and TEXONO nPC-Ge in that order. Similarly, in Fig. 8c, CONNIE sets the strongest limit for the scalar case in the low mediator mass regime, followed by Dresden-II. The subsequent limits are given by TEXONO pPC-Ge, CONUS, TEXONO nPC-Ge, and COHERENT, respectively. For the other interaction types, axial-vector, pseudoscalar, and tensor, TEXONO pPC-Ge demonstrates a clear advantage over COHERENT in the low-mass region. For higher mediator mass regime, however, COHERENT experiments provide the tightest bounds among all interaction types. It is also observed that TEXONO pPC-Ge experiment shows a significant improvement over TEXONO nPC-Ge experiment.

Due to their lower threshold energies, reactor neutrino experiments offer enhanced sensitivity to light mediators compared to accelerator neutrino experiments, resulting in tighter constraints in the low-mass regime. However, this enhanced sensitivity also changes among different interaction types, as the upper bounds are governed by the unique dependencies of their cross-sections on nuclear recoil energy. For instance, scalar interactions exhibit a cross-section scaling of $\sim 1/T_N$, in contrast to vector interactions, which scale as $\sim 1/T_N^2$. This distinction leads to larger scalar cross-sections relative to the vector cross-sections for the same recoil energy and mediator mass, resulting in more stringent constraints on the cou-

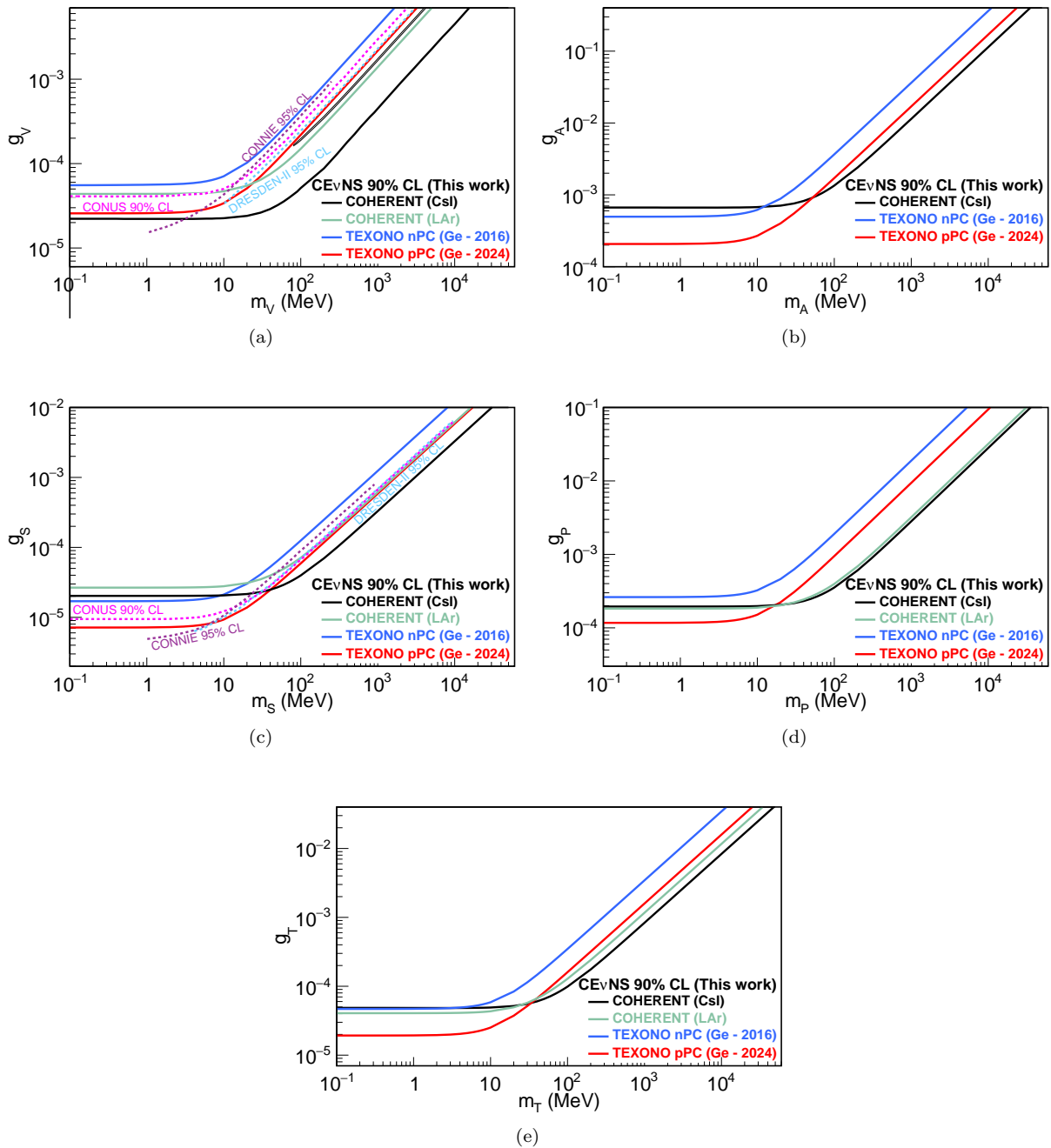


FIG. 8. Bounds at 90% CL are presented for (a) vector, (b) axialvector, (c) scalar, (d) pseudoscalar, and (e) tensor mediator masses and couplings, derived from the TEXONO nPC–Ge and pPC–Ge, and COHERENT CsI(Na) and LAr experiments. These results are compared with global bound from different experiments, including CONUS [49], CONNIE [50], and DRESDEN-II [52], focusing on vector and scalar NSI constraints.

pling constant for scalar interactions. Tensor and vector interactions yield relatively close upper limits due to their similar dependence on $\sim 1/T_N^2$ in the cross-sections. On the other hand, axial-vector interactions are strongly spin-dependent, which leads to notable decreases in the cross-sections and, as a result, weaker upper bounds. To illustrate, COHERENT LAr experiment is unable to pro-

vide any limits in axial vector type interaction, as Ar has zero spin contribution to the cross-section. In the case of pseudoscalar interactions, the cross-sections behaves as $\sim T_N^2/(2m_N T_N + m_P^2)^2$, which diminish sharply at low recoil energies, resulting in weaker constraints compared to other interaction types.

C. Bounds from Model-Independent NSI

Table III presents the best-fit measurement results and corresponding limits at 90% CL for individual epsilon parameters in the TEXONO nPC–Ge and pPC–Ge experiments, while Table IV provides the respective sensitivities for the COHERENT CsI(Na) and LAr experiments. This analysis assumes a scenario where only one parameter is nonzero at a time, with all other parameters set to zero. The tables display the parameter limits for all possible NSI scenarios, distinguishing between FC (diagonal) and FV (off-diagonal) cases. As in the simplified model, five types of interactions are considered: vector, axial vector, scalar, pseudoscalar, and tensor, with couplings denoted as $\varepsilon_{\alpha\beta}^{fX}$, where $f = u, d$; $\alpha, \beta = e, \mu, \tau$; and $X = V, A, S, P$, and T . However, the CE ν NS measurements from the TEXONO and COHERENT experiments are unable to constrain all parameters due to the different compositions of incoming the neutrino beams. The SNS neutrino flux includes three components (ν_e, ν_μ , and $\bar{\nu}_\mu$), enabling coherent scattering across all scenarios with ν_e and ν_μ . In contrast, the reactor neutrino flux contains only a single component ($\bar{\nu}_e$), allowing coherent scattering solely with electron neutrinos. Additionally, we assume that the epsilon parameters are real and impose the hermiticity condition $\varepsilon_{\beta\alpha}^{fX} \equiv (\varepsilon_{\alpha\beta}^{fX})^*$, which leads to six independent parameters per quark flavor. However, only five of these can be constrained by the SNS neutrino fluxes, while only two can be constrained by the reactor neutrino flux. Except for vector NSI, the FC and certain FV couplings are expected to be identical (i.e., $\varepsilon_{ee}^{fX} = \varepsilon_{e\tau}^{fX}$ and $\varepsilon_{\mu\mu}^{fX} = \varepsilon_{\mu\tau}^{fX}$). This equivalence arises because the strength of the FC coupling on nuclei corresponds to that of the FV parameter, due to the absence of interference between NSI and the SM and their dependence on the same flux term.

Taking all factors into consideration, the relevant coupling parameters in the TEXONO experiment are ε_{ee}^{fX} for the FC case and $\varepsilon_{e\mu(\tau)}^{fX}$ for the FV case. In the COHERENT experiment, the relevant parameters are ε_{ee}^{fX} and $\varepsilon_{\mu\mu}^{fX}$ for the FC case, and $\varepsilon_{e\mu(\tau)}^{fX}$ and $\varepsilon_{\mu\tau}^{fX}$ for the FV case. For vector NSI, both the COHERENT CsI(Na) and LAr experiments exhibit two degenerate minima in the FC scenario, caused by interference between the SM and NSI contributions to the CE ν NS cross-section. This interference leads to an almost complete cancellation of the SM and NSI contributions, resulting in a significant reduction in the predicted CE ν NS event rate.

As summarized in Table IV, flavor-diagonal vector couplings provide tighter constraints, while flavor-off-diagonal couplings remain less constrained due to the lack of interaction with the SM. This behavior also allows us to provide only upper limits for flavor-off-diagonal parameters, rather than well-defined allowed regions observed for flavor-diagonal parameters. NSI couplings associated with the other interaction types – A, S, P, and T – are similarly constrained as flavor-off-diagonal vec-

tor couplings, because they do not exhibit interference with the SM. In general, the constraints vary depending on the neutrino flavors involved in the interaction. This is because having multiple neutrino flavors in the flux enhances the sensitivity to NSI parameters, with each flavor contributing unique interaction rates, cross-section dependencies, and interference effects. This enables the experiment to investigate interactions associated with the individual neutrino flavors, thereby increasing its statistical power. For instance, $\varepsilon_{e\mu}^{uX}$, which includes all components of the SNS flux, provides more tight bound compared to ε_{ee}^{uX} , which only includes the ν_e flux. Consequently, experiments like COHERENT, using mixed neutrino flux from the SNS, are more effective in breaking degeneracies and placing tighter constraints on both flavor-diagonal and flavor-off-diagonal NSI parameters than reactor-based experiments with a single-neutrino flavor. In this regard, we observe in Table III that the TEXONO experiments generally yield less stringent bounds compared to the COHERENT CsI(Na) and LAr experiments. However, a notable exception is observed in axial-vector interactions, where the different spin contributions of target nuclei to the cross-sections in the corresponding experiments lead TEXONO pPC–Ge to provide tighter constraints than COHERENT CsI(Na), while COHERENT LAr is unable to set any limits due to the spin-independence of its cross-section. In addition, reactor neutrino experiments face challenges in exploring various NSI parameters due to their reliance on a single-flavor neutrino flux and the limitations in experiment sensitivity, resulting in fewer constrained NSI coupling parameters than accelerator neutrino experiments. However, with advancements in detection thresholds, background suppression, and experimental techniques, reactor neutrino experiments could achieve CE ν NS detection and significantly improve their sensitivity to NSI parameters in the future.

We further explore the sensitivities to pairs of NSI parameters. While a wide variety of NSI parameter pairs can be analysed, our study is limited to a few illustrative cases. These selected examples effectively capture the key features and trends observed across the parameter space. The allowed regions for other parameter combinations generally exhibit similar behavior. By focusing on these representative cases, we provide a clear and concise overview of the parameter space, minimizing redundancy and ensuring the clarity and consistency in this work. In Figs. 9 – 11, we present the 90% CL upper bounds for all possible flavor-diagonal (FC) and flavor-off-diagonal (FV) cases of vector NSI interactions, respectively. Fig. 9 focuses on flavor-diagonal interactions, with the upper panel showing limits for scenarios involving a single flavor-diagonal term (e.g., $\varepsilon_{ee(\mu\mu)}^{uV} - \varepsilon_{ee(\mu\mu)}^{dV}$), while the lower panel illustrates the parameter space limits for combinations of two flavor-diagonal terms, such as $(\varepsilon_{ee}^{fV} - \varepsilon_{\mu\mu}^{fV})$. In the $(\varepsilon_{ee(\mu\mu)}^{uV} - \varepsilon_{ee(\mu\mu)}^{dV})$ parameter space, the constraints manifest as parallel bands. Conversely, in the $(\varepsilon_{ee}^{qV} - \varepsilon_{\mu\mu}^{qV})$ parameter space, the allowed regions

TABLE III. Summary of the best-fit parameter values (BFPVs) and corresponding limits at 1σ and 90% CL for vector, axial-vector, scalar, pseudo-scalar, and tensor type NSI measurements, based on one-parameter-at-a-time analysis. The results are presented in comparison with two datasets from the TEXONO Collaboration: the 2016 dataset obtained with the nPC–Ge detector and the 2024 dataset obtained with the pPC–Ge detector. Here only one coupling parameter is assumed to be non-zero for each bound.

Fitting Par	TEXONO nPC–Ge			TEXONO pPC–Ge		
	BFPV $\pm 1\sigma$	90% CL	χ^2/dof	BFPV $\pm 1\sigma$	90% CL	χ^2/dof
ε_{ee}^{uV}	0.18 ± 1.565	$-1.90 < \varepsilon_{ee}^{uV} < 2.276$	81.4/120	$0.0008_{-0.154}^{+0.526}$	$-0.222 < \varepsilon_{ee}^{uV} < 0.597$	87.87/79
ε_{ee}^{dV}	0.17 ± 1.445	$-1.76 < \varepsilon_{ee}^{dV} < 2.10$	81.4/120	$0.0008_{-0.142}^{+0.486}$	$-0.206 < \varepsilon_{ee}^{dV} < 0.552$	87.87/79
$(\varepsilon_{e\mu(\tau)}^{uV})^2$	-0.67 ± 3.005	$\varepsilon_{e\mu(\tau)}^{uV} < 2.070$	81.3/120	-0.0004 ± 0.081	$\varepsilon_{e\mu(\tau)}^{uV} < 0.364$	87.87/79
$(\varepsilon_{e\mu(\tau)}^{dV})^2$	-0.57 ± 2.568	$\varepsilon_{e\mu(\tau)}^{dV} < 1.912$	81.3/120	-0.0004 ± 0.069	$\varepsilon_{e\mu(\tau)}^{dV} < 0.337$	87.87/79
$(\varepsilon_{ee(\mu;\tau)}^{uA})^2$	-1284 ± 5900	$\varepsilon_{ee(\mu;\tau)}^{uA} < 91.85$	81.3/120	13.2 ± 240.2	$\varepsilon_{ee(\mu;\tau)}^{uA} < 20.23$	87.86/79
$(\varepsilon_{ee(\mu;\tau)}^{dA})^2$	-274.0 ± 1267	$\varepsilon_{ee(\mu;\tau)}^{dA} < 42.54$	81.3/120	2.82 ± 51.53	$\varepsilon_{ee(\mu;\tau)}^{dA} < 9.369$	87.86/79
$(\varepsilon_{ee(\mu;\tau)}^{uS})^2$	-0.0047 ± 0.022	$\varepsilon_{ee(\mu;\tau)}^{uS} < 0.176$	81.3/120	$(5.4 \pm 90.1) \times 10^{-5}$	$\varepsilon_{ee(\mu;\tau)}^{uS} < 0.039$	87.86/79
$(\varepsilon_{ee(\mu;\tau)}^{dS})^2$	-0.0063 ± 0.029	$\varepsilon_{ee(\mu;\tau)}^{dS} < 0.204$	81.3/120	$(0.74 \pm 12.2) \times 10^{-4}$	$\varepsilon_{ee(\mu;\tau)}^{dS} < 0.046$	87.86/79
$(\varepsilon_{ee(\mu;\tau)}^{uP})^2$	-106.0 ± 491.4	$\varepsilon_{ee(\mu;\tau)}^{uP} < 26.53$	81.3/120	2.53 ± 24.93	$\varepsilon_{ee(\mu;\tau)}^{uP} < 6.601$	87.85/79
$(\varepsilon_{ee(\mu;\tau)}^{dP})^2$	-2340 ± 10855	$\varepsilon_{ee(\mu;\tau)}^{dP} < 124.7$	81.3/120	56.0 ± 551	$\varepsilon_{ee(\mu;\tau)}^{dP} < 31.03$	87.85/79
$(\varepsilon_{ee(\mu;\tau)}^{uT})^2$	-0.51 ± 2.314	$\varepsilon_{ee(\mu;\tau)}^{uT} < 1.819$	81.3/120	0.0040 ± 0.088	$\varepsilon_{ee(\mu;\tau)}^{uT} < 0.387$	87.86/79
$(\varepsilon_{ee(\mu;\tau)}^{dT})^2$	-0.22 ± 0.995	$\varepsilon_{ee(\mu;\tau)}^{dT} < 1.193$	81.3/120	0.0018 ± 0.038	$\varepsilon_{ee(\mu;\tau)}^{dT} < 0.254$	87.86/79

form elliptical contours. For certain cases, particularly with the CsI target, degenerate regions emerge due to interference between the SM and NSI differential cross-sections. These degeneracies are exclusive to vector interactions. This behavior is a consequence of the dependence of the cross-section on specific linear combinations of the parameters, as derived from Eqs.(2.25), and Eq. (2.26). Specifically, the cross-section depends on the condition $\varepsilon_{ee}^{uV}(2Z + N) + \varepsilon_{ee}^{dV}(Z + 2N) = \text{constant}$, resulting in two allowed bands with slopes determined by the ratio $(2Z + N)/(Z + 2N)$ [40, 60].

The elliptical contours observed in the lower panel of Fig. 9 arise from the interference of parameters associated with two distinct neutrino flavors in the SM. This behavior is described by the equation $[(2Z + N)\varepsilon_{ee}^{uV} + Q_{\text{SM}_V}]^2 + [(2Z + N)\varepsilon_{\mu\mu}^{uV} + Q_{\text{SM}_V}]^2 = \text{constant}$, which clearly represents the equation of an ellipse. As a result, all combinations of $(\varepsilon_{ee}^{qV} - \varepsilon_{\mu\mu}^{qV})$ that produce in the same differential event rates within a specific energy range create a degenerate region, similar to the single-flavor FC case. However, instead of appearing as parallel bands, this degeneracy manifests as a smaller ellipse. Additionally, since reactor neutrino experiments involve a single neutrino flavor flux, the TEXONO experiments can only provide constraints in the $(\varepsilon_{ee}^{qV} - \varepsilon_{ee}^{qV})$ parameter space. As expected, these limits are less restrictive than those derived from the COHERENT experiments, which involve three neutrino fluxes.

In Figs. 10 and 11, we present the 90% CL upper limits for selected flavor-off-diagonal (FV) cases. For these scenarios, we explored three different parameter spaces: combinations of $\varepsilon_{\alpha\beta}^{uV} - \varepsilon_{\alpha\beta}^{dV}$ in Fig. 10, and $\varepsilon_{\alpha\alpha}^{qV} - \varepsilon_{\alpha\beta}^{qV}$, and $\varepsilon_{\alpha\beta}^{qV} - \varepsilon_{ij}^{qV}$, where $\alpha\beta \neq ij$, in Fig. 11. In the case of a single flavor-off-diagonal parameter spaces, as shown in Fig. 10, the cross-section takes the form $\varepsilon_{\alpha\beta}^{uV}(2Z + N) + \varepsilon_{\alpha\beta}^{dV}(Z + 2N) = \text{constant}$, with a center at $(0,0)$, and the upper limits form parallel bands. However, unlike the flavor-diagonal case, there is no SM interference term so no degeneracy region is observed for CsI. Instead, the bounds formed tighter single bands. The width of these bands is determined by the flux term involved in the interaction. The tightest bound is obtained for the parameter space $\varepsilon_{e\mu}^{uV} - \varepsilon_{e\mu}^{dV}$, which includes three types of flux from SNS. On the other hand, the least restrictive bound is obtained for the parameter space $\varepsilon_{e\tau}^{uV} - \varepsilon_{e\tau}^{dV}$, which induces only the electron neutrino flux. As mentioned earlier, while the TEXONO pPC–Ge experiment provides much more stringent limits than nPC–Ge, both still remain less restrictive than COHERENT due to the lower SM event rate. Additionally, due to the presence of only a single type of neutrino flux in the interaction, no bound for the parameter space $\varepsilon_{\mu\tau}^{uV} - \varepsilon_{\mu\tau}^{dV}$ can be determined in the TEXONO experiments. For the same reason, the TEXONO bounds in Figs. 10a and 10b produce identical contours.

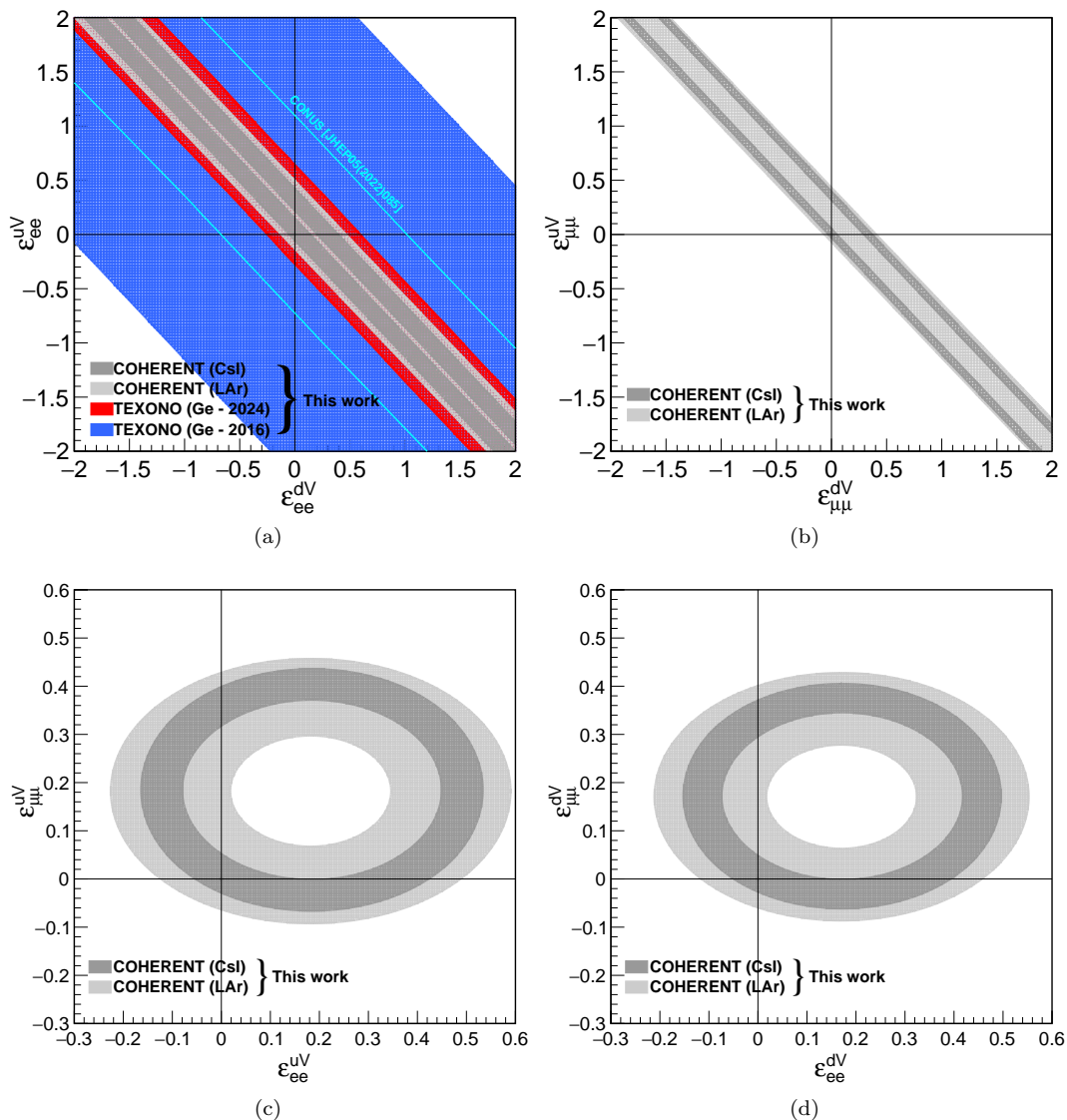


FIG. 9. The 90% CL allowed region in the $\varepsilon_{ee}^{dV} - \varepsilon_{ee}^{uV}$, $\varepsilon_{\mu\mu}^{dV} - \varepsilon_{\mu\mu}^{uV}$, $\varepsilon_{ee}^{uV} - \varepsilon_{\mu\mu}^{uV}$, and $\varepsilon_{ee}^{dV} - \varepsilon_{\mu\mu}^{dV}$ parameter spaces for vector-type NSI in the FC case.

In some FV cases, when two flavor-off-diagonal parameter spaces or a combination of one flavor-diagonal and one flavor-off-diagonal parameter space are considered, and the SM interference terms are absent while the first-order terms of the relevant epsilon parameters do not appear in the cross-section, the upper limits cannot be directly set on the parameters. Instead, as shown in Figs. 11a and 11c, the χ^2 analysis is performed on the epsilon-squared parameters, where $(\varepsilon_{\alpha\beta}^{qV})^2 > 0$, and then subsequently converted into the $\varepsilon_{\alpha\beta}^{qV}$ parameter space. This method allows us to eliminate certain regions of the full elliptical bounds, resulting in semi-elliptical (Fig. 11b) or quarter-elliptical (Fig. 11d) bounds. Furthermore, an elliptical degeneracy region is also observed in Fig. 11b, although it is smaller compared to the one in Fig. 9c. This difference arises because, while ε_{ee}^{uV} still in-

terferes with the SM cross-section, leading to destructive CE ν NS events, the $\varepsilon_{e\mu}^{uV}$ term does not exhibit any interference with the SM. The absence of interference contributes to the CE ν NS signal, partially compensating for the destructive interference, but it does not completely break the degeneracy. Finally, the analyses of other FV parameter spaces in Fig. 11 follow a similar methodology. To ensure clarity and provide a more concise representation, plots related to the epsilon-squared, $(\varepsilon_{\alpha\beta}^{qV})^2$, are excluded and only the corresponding $\varepsilon_{\alpha\beta}^{qV}$ parameter spaces are displayed.

In Figs. 12 and 13, we present the 90% CL upper limits of axial-vector interactions in possible FC and FV scenarios. The cross-section for this type of interaction also exhibits a specific linear combination of the relevant epsilon parameters, given by $\varepsilon_{\alpha\beta}^{uA}(\mathcal{N}S_n\Delta_u^n +$

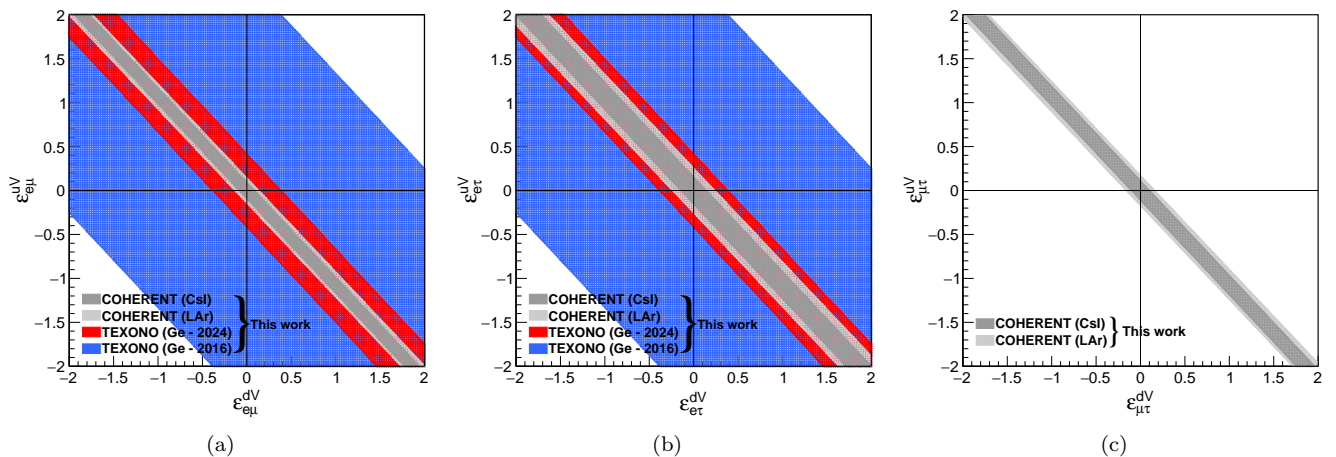


FIG. 10. The 90% CL allowed region in the $\varepsilon_{e\mu}^{dV} - \varepsilon_{e\mu}^{uV}$, $\varepsilon_{e\tau}^{dV} - \varepsilon_{e\tau}^{uV}$, and $\varepsilon_{\mu\tau}^{dV} - \varepsilon_{\mu\tau}^{uV}$ parameter spaces for vector-type NSI in the FV case.

$ZS_p\Delta_u^p + \varepsilon_{\alpha\beta}^{dA}(\mathcal{N}S_n\Delta_d^n + ZS_p\Delta_d^p) = \text{constant}$, as shown in Eq.(2.27). Although this linear dependence differs from that observed in the vector case, the resulting upper bounds still appear as linear bands, but with a different slope, centred symmetrically at $(0,0)$ in parameter space. In this linear expression, S_p and S_n are spin-related parameters that dictate the slope of the bands through their significant effects on the cross-section of the axial-vector interaction type. There is no axial-vector contribution for Ar atom, as it has even numbers of protons and neutrons, making it impossible to set any upper limits for axial-vector type interactions with the COHERENT LAr experiment. In contrast, for CsI(Na) and Ge target nuclei, the contributions to the axial-vector cross-sections are determined based on the axial-vector parameters provided in Table I and spin expectation values discussed in previous sections. Considering the effects of all these parameters, we observe that the down-quark-related terms dominate the CsI(Na) and Ge cross-sections, yielding tighter bounds for interaction scenarios involving only down-quarks (i.e. $\varepsilon_{ee}^{dA} - \varepsilon_{e\tau}^{dA}$). On the other hand, in some scenarios involving only-up-quarks (i.e. $\varepsilon_{ee}^{uA} - \varepsilon_{e\tau}^{uA}$), TEXONO pPC-Ge provides stricter limits than COHERENT, since the contribution to the CsI(Na) cross-section is much smaller compared to Ge. The asymmetry observed between the allowed bands for COHERENT and TEXONO in Figs. 12a and 12c also arises from the varying dominance of up-quark and down-quark terms in cross-sections. In Fig. 12b, similar to the vector interaction case, upper limits could not be determined for TEXONO due to its single-type neutrino flux. The limits shown in Fig. 13, includes parameter spaces for three scenario: two different flavor-diagonal, one flavor-diagonal and one flavor-off-diagonal, and two different flavor-off-diagonal scenarios. All of these result in quarter-elliptical regions. To derive these limits, we begin with the epsilon-squared parameter space, $(\varepsilon_{\alpha\beta}^{fA})^2$, as explained above, and then transition to the epsilon

parameter space, $\varepsilon_{\alpha\beta}^{fA}$.

In contrast to the vectorial case, the axial-vector case does not involve interference with the SM, allowing certain FC and FV scenarios to produce similar event numbers when the epsilon parameters are influenced by the same neutrino fluxes. This results in identical upper limits for certain parameter spaces thereby reducing the number of parameter spaces in which upper limits can be set, particularly in the case of the TEXONO experiment, which is induced exclusively by single neutrino flux. For instance, in Figs. 13a and 13b, it can be seen that the contributions to the number of events from the flavor-diagonal ε_{ee}^{qA} term and the flavor-off-diagonal $\varepsilon_{e\tau}^{qA}$ terms yield the same limits, as both are related to the electron (or muon) neutrino flux. A similar behavior is also observed in Figs. 12e and 12f between $\varepsilon_{ee}^{qA} - \varepsilon_{\mu\mu}^{qA}$ and $\varepsilon_{e\tau}^{qA} - \varepsilon_{\mu\tau}^{qA}$ parameter spaces. Additionally, one can observe that the limits provided by the parameter spaces $\varepsilon_{ee}^{uA} - \varepsilon_{e\tau}^{uA}$ and $\varepsilon_{e\mu}^{uA} - \varepsilon_{e\tau}^{uA}$ in Figs. 13a and 13c, as well as $\varepsilon_{ee}^{dA} - \varepsilon_{e\tau}^{dA}$ and $\varepsilon_{e\mu}^{dA} - \varepsilon_{e\tau}^{dA}$ in Figs. 13b and 13d, are identical for TEXONO, due to its single-type neutrino flux.

Having discussed axial-vector NSI, we now turn to examine the corresponding behavior in scalar and pseudoscalar types of NSI. Figs. 14 and 15 show the 90% CL bounds for scalar interactions in all possible FC and FV scenarios, Figs. 16 and 17 present the pseudoscalar case. As in the axial vector case, the scalar and pseudoscalar interactions also involve similar evaluations of epsilon parameters, but there are important differences in how these interactions behave. The cross-section for scalar interactions is expressed as a linear combination of the relevant epsilon parameters, formulated as $\varepsilon_{\alpha\beta}^{uS}[\mathcal{N}(m_n/m_u)f_{Tu}^n + \mathcal{Z}(m_p/m_u)f_{Tu}^p] + \varepsilon_{\alpha\beta}^{dS}[\mathcal{N}(m_n/m_d)f_{Td}^n + \mathcal{Z}(m_p/m_d)f_{Td}^p] = \text{constant}$, as derived in Eq.(2.28). For pseudoscalar interactions, the cross-section is similarly represented as a linear combina-

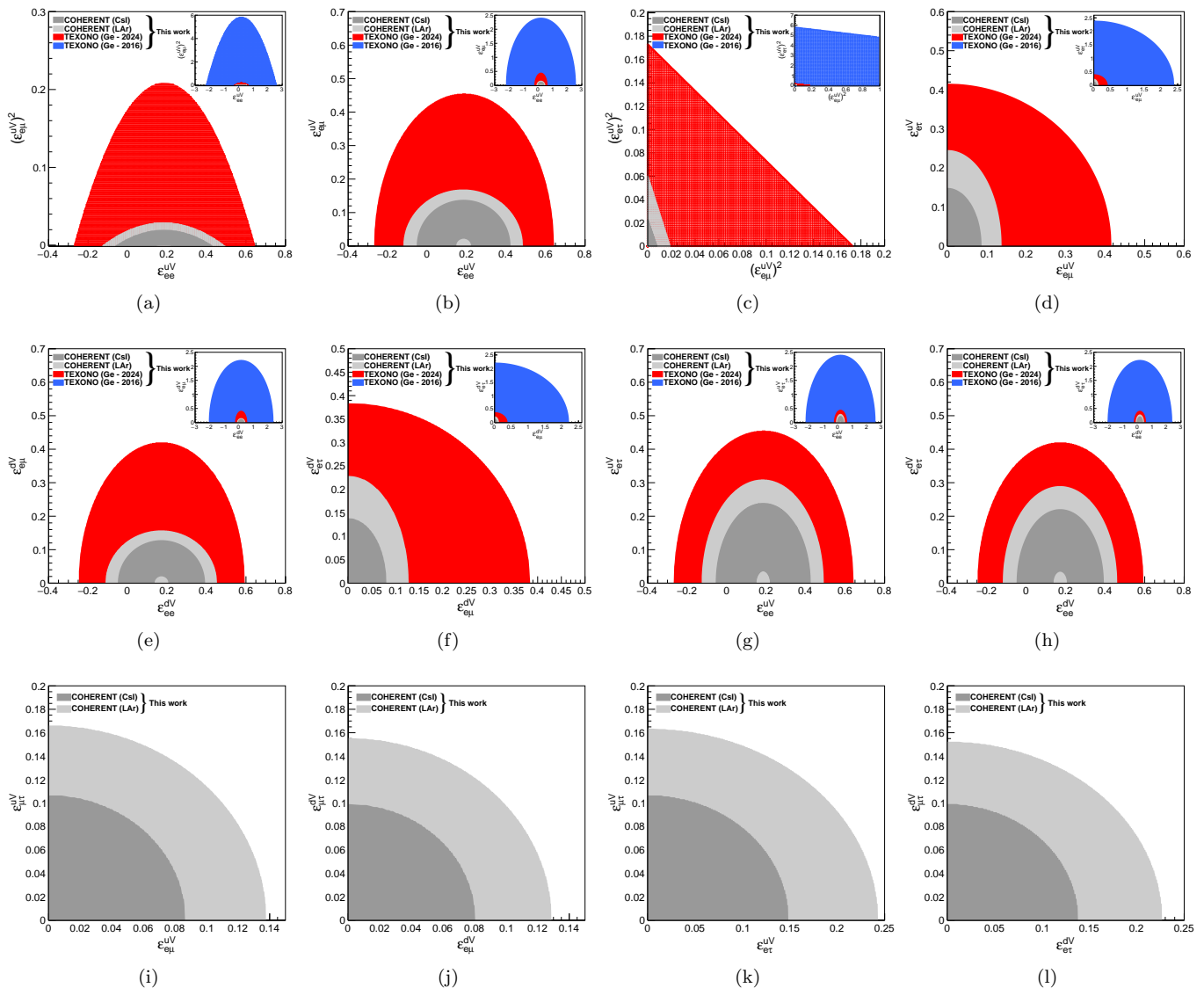


FIG. 11. The 90% CL allowed region in the following parameter spaces for vector-type NSI in the FV case: $\epsilon_{ee}^{uV} - (\epsilon_{e\mu}^{uV})^2$, $\epsilon_{ee}^{uV} - \epsilon_{e\mu}^{uV}$, $(\epsilon_{e\mu}^{uV})^2 - (\epsilon_{e\tau}^{uV})^2$, $\epsilon_{e\mu}^{uV} - \epsilon_{e\tau}^{uV}$, $\epsilon_{ee}^{dV} - \epsilon_{e\mu}^{dV}$, $\epsilon_{e\mu}^{dV} - \epsilon_{e\tau}^{dV}$, $\epsilon_{ee}^{uV} - \epsilon_{e\tau}^{uV}$, $\epsilon_{ee}^{dV} - \epsilon_{e\tau}^{dV}$, $\epsilon_{e\mu}^{uV} - \epsilon_{e\mu}^{dV}$, $\epsilon_{e\mu}^{uV} - \epsilon_{e\tau}^{dV}$, $\epsilon_{e\mu}^{dV} - \epsilon_{e\tau}^{dV}$, $\epsilon_{e\tau}^{uV} - \epsilon_{e\mu}^{dV}$, and $\epsilon_{e\tau}^{dV} - \epsilon_{e\mu}^{dV}$.

tion of the corresponding epsilon parameters, as shown in the equation: $\epsilon_{\alpha\beta}^{uP}[\mathcal{N}(m_n/m_u)h_u^n + \mathcal{Z}(m_p/m_u)h_u^p] + \epsilon_{\alpha\beta}^{dP}[\mathcal{N}(m_n/m_d)h_d^n + \mathcal{Z}(m_p/m_d)h_d^p] = \text{constant}$, as given in Eq.(2.29). Although the axialvector, scalar, and pseudoscalar cases all show a linear dependence of the bounds on the epsilon parameters, the unique features of scalar and pseudoscalar interactions cause differences in the slope of the linear bands formed by the parameters that affect the cross-section with the corresponding values provided in Table I.

In all three interactions, both axialvector and pseudoscalar interactions result in less stringent constraints, while the pseudoscalar interactions generally producing weaker bounds. Although both are spin-dependent in-

teractions, the spin dependence is less notable in the pseudoscalar case, whereas the axial-vector cross-section depends strictly on spin contributions and the spin expectation values of each nucleus. This dependency can significantly impact the upper bounds. For example, in the case of COHERENT CsI, the pseudoscalar interaction generally provides more stringent bounds compared to the axial-vector interaction. In contrast, the TEXONO experiment shows various behavior: while it offers better limits for pseudo-scalar interactions in up-quark-related parameter spaces, it provides tighter bounds for axial-vector interactions in down-quark-related parameter spaces. Specifically, for axial-vector interactions, no bounds can be determined for LAR due to its zero spin contribution, as mentioned above. In contrast,

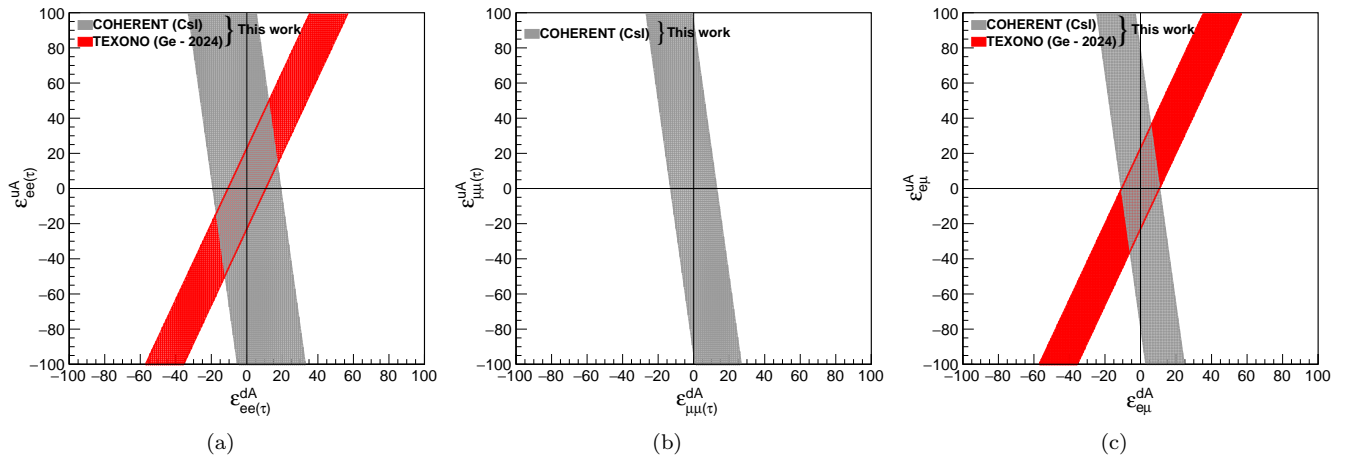


FIG. 12. The 90% CL allowed region in the parameter spaces $\epsilon_{ee}^{dA} - \epsilon_{ee}^{uA}$, $\epsilon_{\mu\mu}^{dA} - \epsilon_{\mu\mu}^{uA}$, and $\epsilon_{e\mu}^{dA} - \epsilon_{e\mu}^{uA}$ for axialvector type NSI in the single-type flavor-diagonal scenario (a) and (b), and single-type flavor-off-diagonal scenario (c).

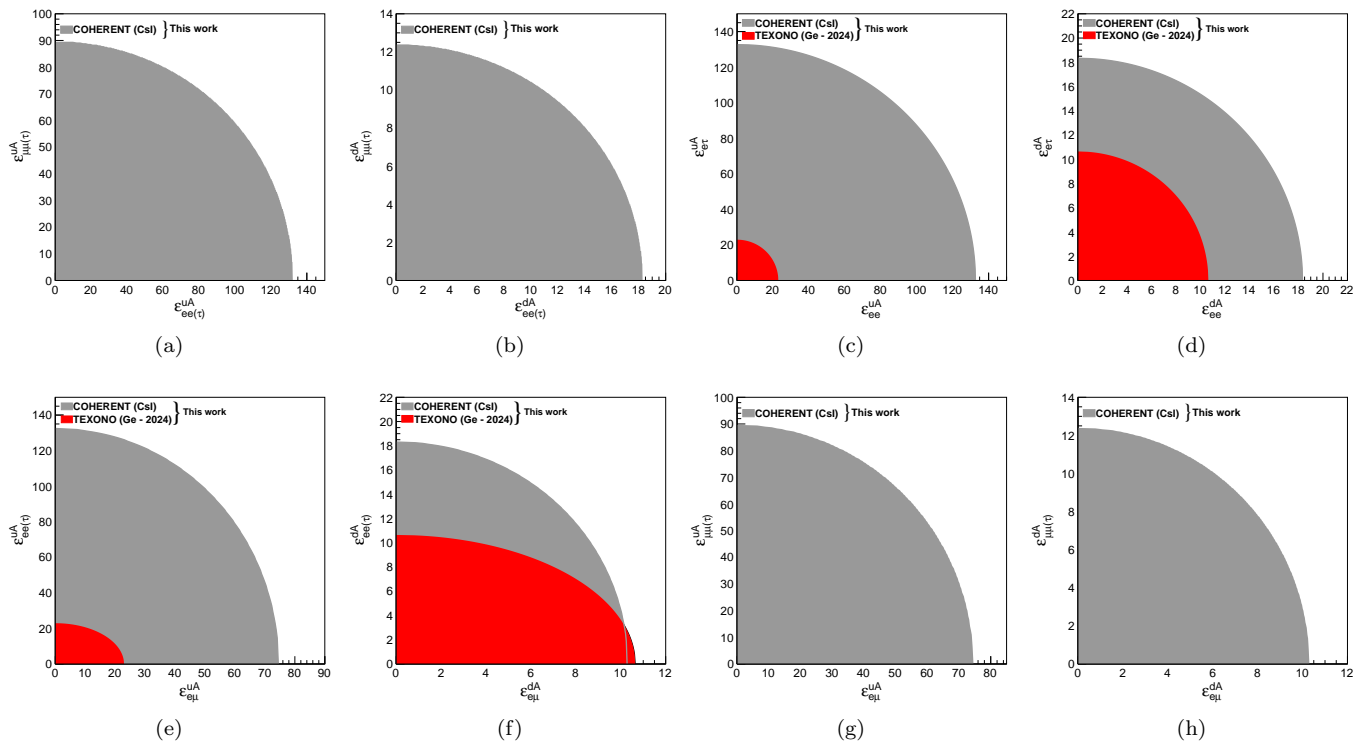


FIG. 13. The 90% CL allowed region in the parameter spaces $\epsilon_{ee}^{uA} - \epsilon_{\mu\mu}^{uA}$, $\epsilon_{ee}^{dA} - \epsilon_{\mu\mu}^{dA}$, $\epsilon_{ee}^{uA} - \epsilon_{e\tau}^{uA}$, $\epsilon_{ee}^{dA} - \epsilon_{e\tau}^{dA}$, $\epsilon_{e\mu}^{uA} - \epsilon_{e\mu}^{dA}$, $\epsilon_{e\mu}^{dA} - \epsilon_{\mu\mu}^{dA}$, and $\epsilon_{e\mu}^{uA} - \epsilon_{\mu\mu}^{uA}$ for axialvector type NSI in the following scenarios: two different flavor-diagonal (a) and (b), one flavor-diagonal and one flavor-off-diagonal (c) and (d), and two different flavor-off-diagonal (e), (f), (g), and (h).

pseudoscalar interactions are expected to yield more favourable bounds for LAr targets. Additionally, pseudoscalar interactions are anticipated to give better limits for lighter nuclei than heavier ones, likely due to differences in sensitivity to nuclear mass. As a result, LAr limits tend to provide even better bounds than CsI, as seen in Figs. 16 and 17. Unlike pseudoscalar and axialvector interactions, scalar interactions are spin-independent,

and their cross-section is generally proportional to the nuclear mass. This property leads to stronger bounds for heavier nuclei in the case of scalar interactions. As shown in Figs. 14 and 15, the CsI target provides tighter bounds than LAr. Additionally, compared to both pseudoscalar and axial-vector interactions, scalar interactions yield more stringent bounds, highlighting the importance of nuclear mass in determining the strength of these in-

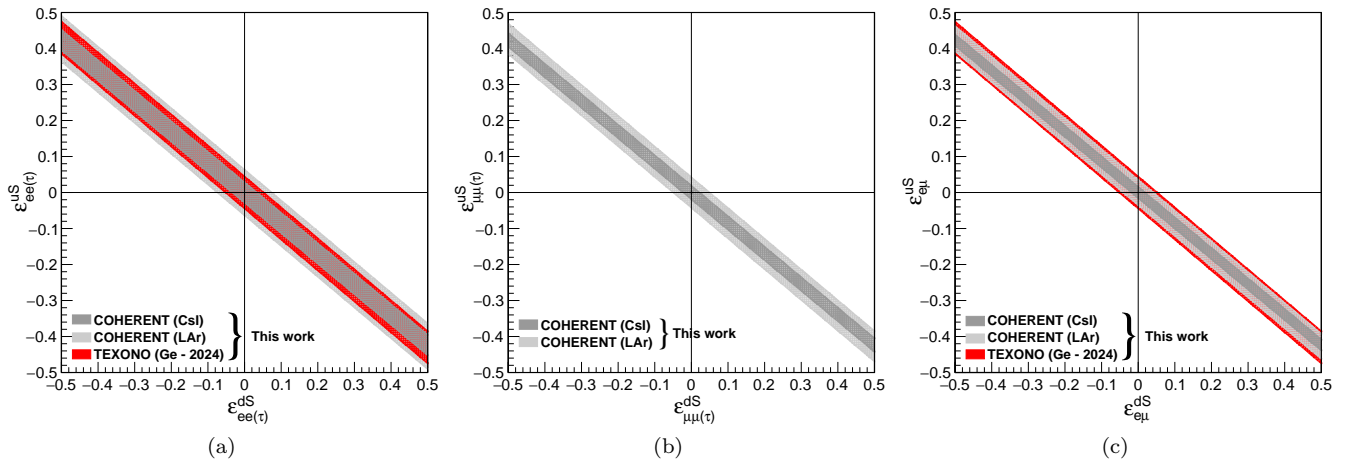


FIG. 14. The 90% CL allowed region in the parameter spaces $\epsilon_{ee(\tau)}^{dS} - \epsilon_{ee(\tau)}^{uS}$, $\epsilon_{\mu\mu(\tau)}^{dS} - \epsilon_{\mu\mu(\tau)}^{uS}$, and $\epsilon_{e\mu}^{dS} - \epsilon_{e\mu}^{uS}$, for scalar-type NSI in the single-type flavor-diagonal scenario (a) and (b), and in single-type flavor-off-diagonal scenario (c).

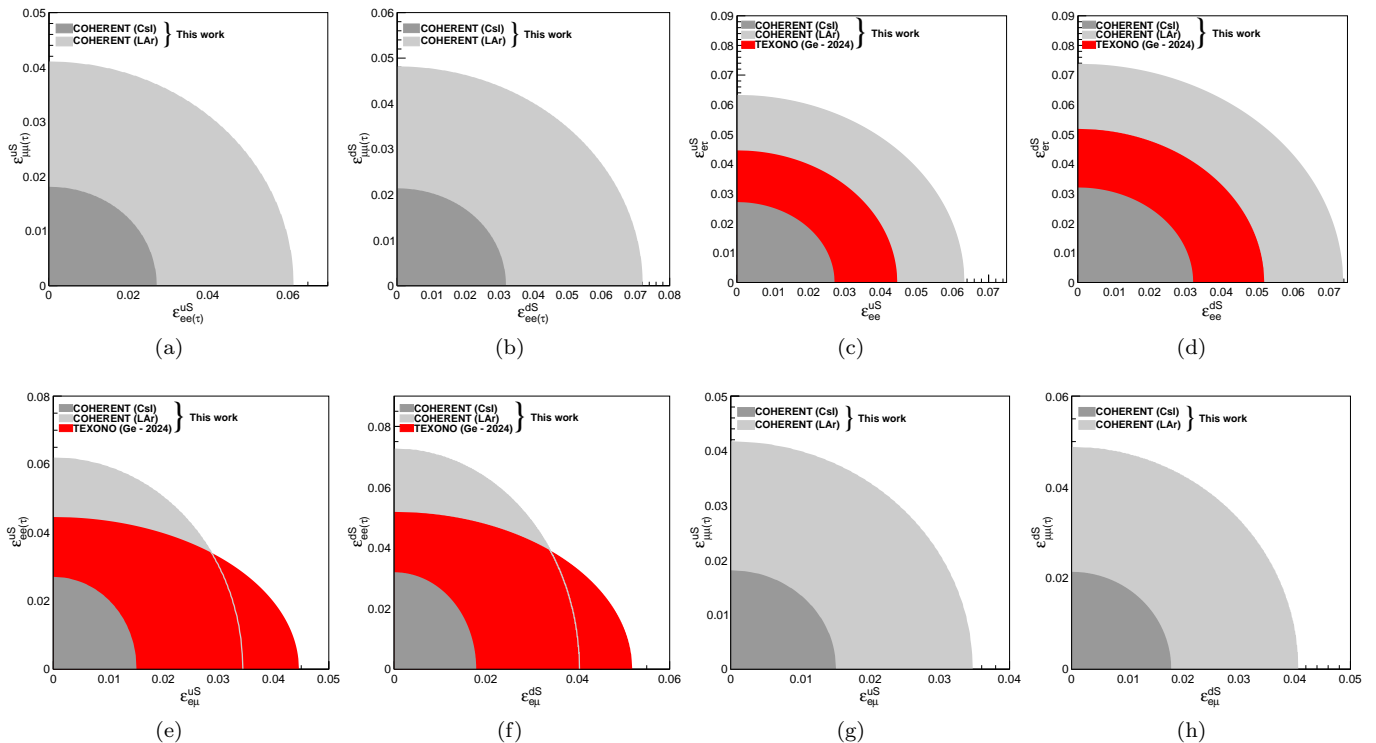


FIG. 15. The 90% CL allowed region in the parameter spaces $\epsilon_{ee(\tau)}^{uS} - \epsilon_{\mu\mu(\tau)}^{uS}$, $\epsilon_{ee(\tau)}^{dS} - \epsilon_{\mu\mu(\tau)}^{dS}$, $\epsilon_{ee}^{uS} - \epsilon_{e\tau}^{uS}$, $\epsilon_{ee}^{dS} - \epsilon_{e\tau}^{dS}$, $\epsilon_{e\mu}^{uS} - \epsilon_{ee(\tau)}^{uS}$, $\epsilon_{e\mu}^{dS} - \epsilon_{ee(\tau)}^{dS}$, $\epsilon_{e\mu}^{uS} - \epsilon_{\mu\mu(\tau)}^{uS}$, and $\epsilon_{e\mu}^{dS} - \epsilon_{\mu\mu(\tau)}^{dS}$ for scalar-type NSI in the following scenarios: two different flavor-diagonal (a) and (b), one flavor-diagonal and one flavor-off-diagonal (c) and (d), and two different flavor-off-diagonal (e), (f), (g), and (h).

teractions. This behavior underscores the unique nature of scalar interactions and their distinct response to different target materials.

As the final point of this section, we present our findings on the upper bounds at 90% CL for tensor-type NSI, as shown in Figs. 18 and 19. To maintain generality, we provide bounds on all possible epsilon parameters. However, it is important to note that, while our

approach does not contradict existing studies, some focus on conditions specific to Majorana neutrinos, which lead to the elimination of certain parameter spaces [60, 98]. The cross-section, like other types of interactions, is generally expressed as a linear combination of the epsilon parameters, as given by the following relation: $\epsilon_{\alpha\beta}^{uT}[\mathcal{N}\delta_u^n + \mathcal{Z}\delta_u^p] + \epsilon_{\alpha\beta}^{dT}[\mathcal{N}\delta_d^n + \mathcal{Z}\delta_d^p] = \text{constant}$. This results in to band-shaped bounds with slopes that dif-

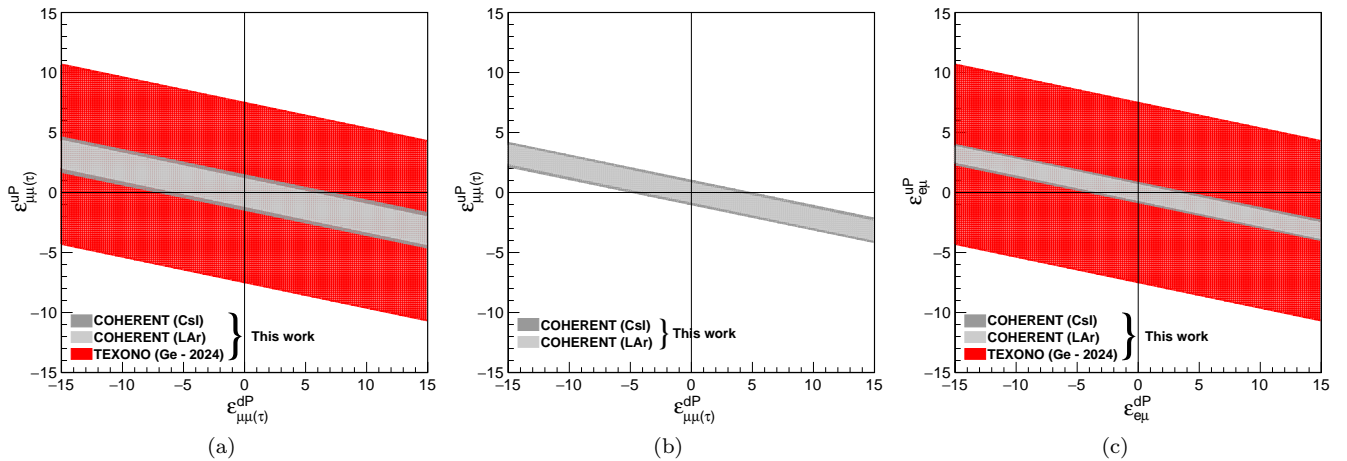


FIG. 16. The 90% CL allowed region of $\varepsilon_{ee}^{dP} - \varepsilon_{ee}^{uP}$, $\varepsilon_{\mu\mu}^{dP} - \varepsilon_{\mu\mu}^{uP}$, and $\varepsilon_{e\mu}^{dP} - \varepsilon_{e\mu}^{uP}$, parameter space for pseudoscalar-type NSI in the single-type flavor-diagonal scenario (a) and (b), and single-type flavor-off-diagonal scenario (c)

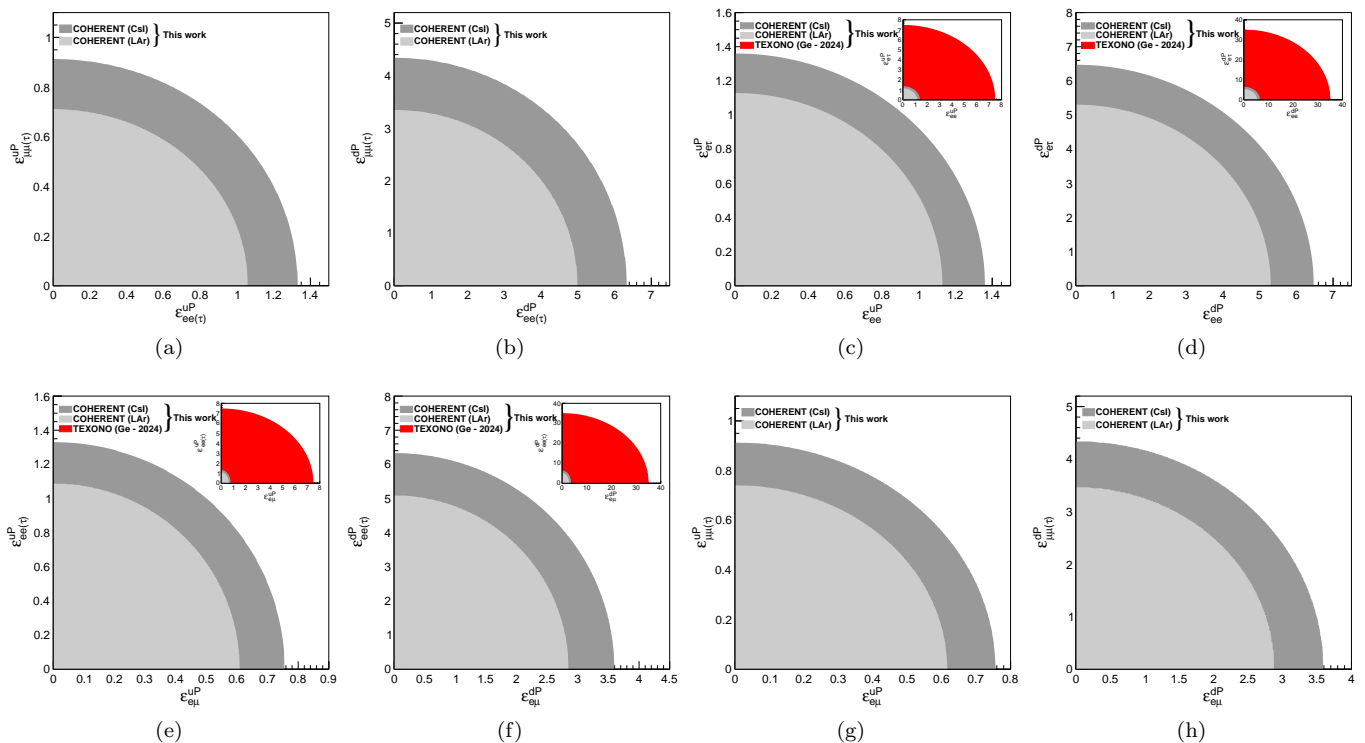


FIG. 17. The 90% CL allowed region of $\varepsilon_{ee}^{uP} - \varepsilon_{\mu\mu}^{uP}$, $\varepsilon_{ee}^{dP} - \varepsilon_{\mu\mu}^{dP}$, $\varepsilon_{ee}^{uP} - \varepsilon_{e\tau}^{uP}$, $\varepsilon_{ee}^{dP} - \varepsilon_{e\tau}^{dP}$, $\varepsilon_{e\mu}^{uP} - \varepsilon_{ee}^{uP}$, $\varepsilon_{e\mu}^{dP} - \varepsilon_{ee}^{dP}$, $\varepsilon_{e\mu}^{uP} - \varepsilon_{\mu\mu}^{uP}$, and $\varepsilon_{e\mu}^{dP} - \varepsilon_{\mu\mu}^{dP}$ parameter space for pseudoscalar type NSI in the two different flavor-diagonal (a) and (b), one flavor-diagonal and one flavor-off-diagonal (c) and (d), and two different flavor-off-diagonal (e), (f), (g), and (h).

fer from those of the scalar case, due to the variation in the parameters appearing in the cross-section. Although tensor interactions exhibit similar behavior to scalar interactions, in that they provide better limits for heavier nuclei, they are less sensitive and result in less stringent limits than scalar interactions.

D. Bounds from Exotic Neutral-Current Interactions

We now turn to the final aspect of our study, presenting results on exotic neutral current interactions of CE ν NS. Based on Eq. (2.34), there are 10 independent parameters dependent on C_X and D_X . However, for sim-

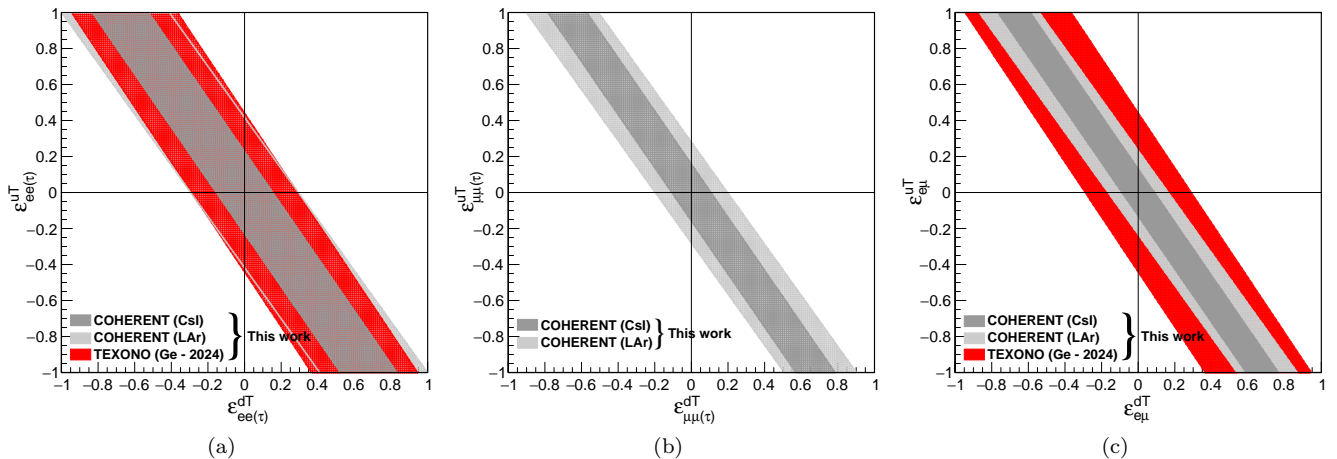


FIG. 18. The 90% CL allowed region of $\varepsilon_{ee(\tau)}^{dT} - \varepsilon_{ee(\tau)}^{uT}$, $\varepsilon_{\mu\mu(\tau)}^{dT} - \varepsilon_{\mu\mu(\tau)}^{uT}$, and $\varepsilon_{e\mu}^{dT} - \varepsilon_{e\mu}^{uT}$ parameter space for tensor-type NSI in the single-type flavor-diagonal scenarios (a) and (b), and single-type flavor-off-diagonal scenario (c).

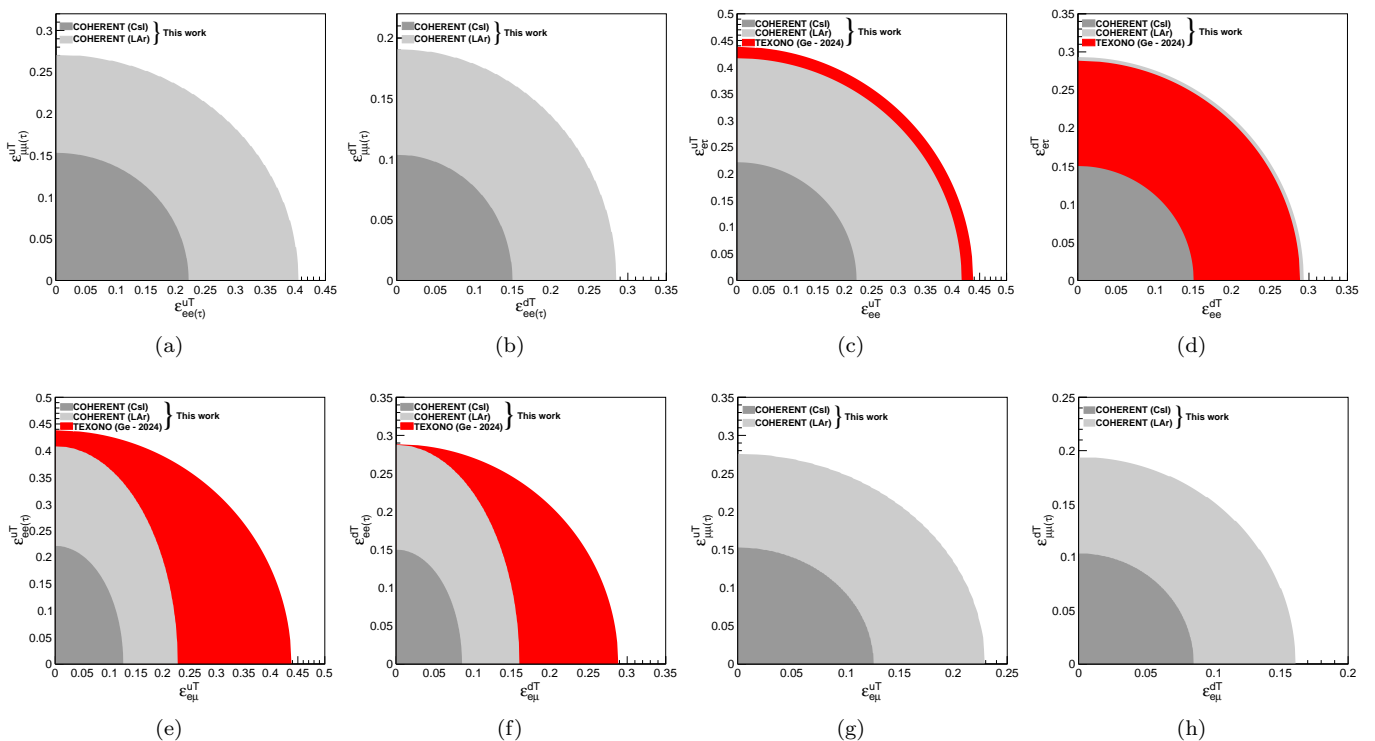


FIG. 19. The 90% CL allowed region of $\varepsilon_{ee(\tau)}^{uT} - \varepsilon_{\mu\mu(\tau)}^{uT}$, $\varepsilon_{ee(\tau)}^{dT} - \varepsilon_{\mu\mu(\tau)}^{dT}$, $\varepsilon_{ee}^{uT} - \varepsilon_{e\tau}^{uT}$, $\varepsilon_{ee}^{dT} - \varepsilon_{e\tau}^{dT}$, $\varepsilon_{e\mu}^{uT} - \varepsilon_{ee(\tau)}^{uT}$, $\varepsilon_{e\mu}^{dT} - \varepsilon_{ee(\tau)}^{dT}$, $\varepsilon_{e\mu}^{uT} - \varepsilon_{\mu\mu(\tau)}^{uT}$, and $\varepsilon_{e\mu}^{dT} - \varepsilon_{\mu\mu(\tau)}^{dT}$ parameter space for tensor-type NSI in the two flavor-diagonal scenarios (a) and (b), one flavor-diagonal and one flavor-off-diagonal scenario (c) and (d), and two flavor-off-diagonal scenarios (e), (f), (g), and (h).

plicity, we make choose to set upper limits on the ξ_X parameters, where $X = V, A, S,$ and T . We present our best-fit measurement results at 1σ and upper limits at 90% CL, assuming only one-parameter remains while setting others zero in Table V and VI for TEXONO and COHERENT experiments, respectively. Similar to the model-independent NSI, the vector term, ξ_V , in this analysis includes interference with the SM. Addi-

tionally, both vector and axial-vector terms also exhibit interference. Therefore, when performing a χ^2 analysis based on a single-parameter scenario, it is possible to set limits directly on the ξ_V term. As shown in the first row of Table VI, the bounds at 90% CL are presented as allowed regions rather than upper limits. For COHERENT CsI(Na) and LAr, two distinct allowed regions are observed, which arise due to the presence of two minima

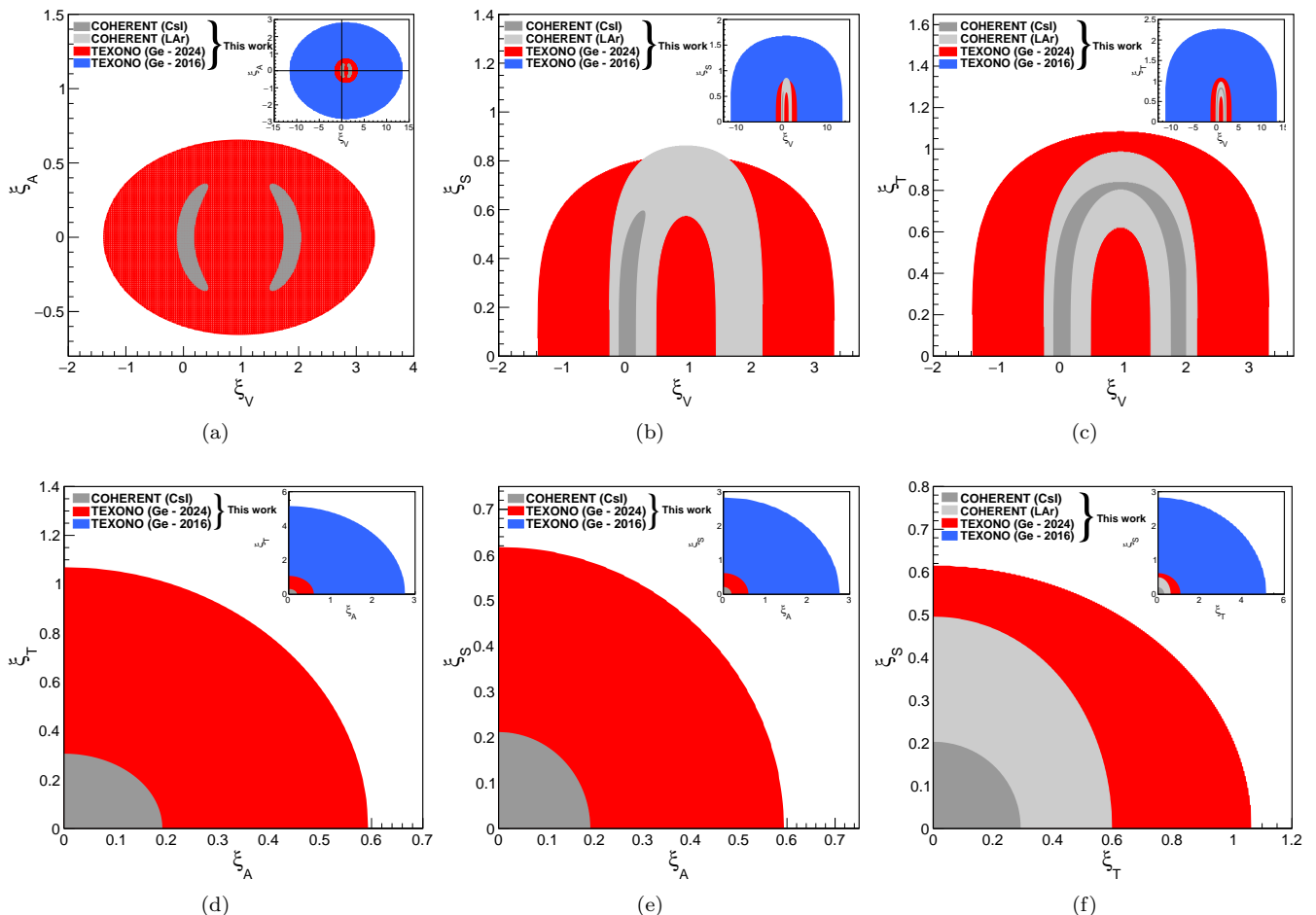


FIG. 20. The 90% CL allowed region of the $\xi_V - \xi_A$, $\xi_V - \xi_S$, $\xi_V - \xi_T$, $\xi_A - \xi_T$, $\xi_A - \xi_S$, and $\xi_T - \xi_S$ parameter spaces for exotic neutral current interactions.

in the χ^2 function. These minima result from degeneracy caused by the SM interference. In comparison, for TEXONO nPC-Ge and pPC-Ge, as seen in Table V, this region is less obvious due to the smaller event rate in the SM, leading to the χ^2 to show a broader region with a single minimum, rather than two minima, and consequently much wider allowed region.

For the parameters ξ_A , ξ_S , and ξ_T , since these parameters appear in the χ^2 function as the square of the parameters, we turn the parameter-square space into the parameter space, similar to the approach used for model-independent NSI. This method allows us to extract upper limits for the parameters at 90% CL. Among these, COHERENT CsI(Na) provides the most stringent bounds, followed by COHERENT LAr, TEXONO pPC-Ge, and TEXONO nPC-Ge, respectively. In Fig. 20, we present the 90% CL upper bounds for the 2-parameter scenario across six possible parameter spaces: $\xi_V - \xi_A$, $\xi_V - \xi_S$, $\xi_V - \xi_T$, $\xi_A - \xi_T$, $\xi_A - \xi_S$, and $\xi_T - \xi_S$.

Unlike the simpler one-parameter case, the two-parameter scenario involves more complex interactions between the parameters, leading to changes in the struc-

ture of the allowed regions. The interference between vector term and both the SM and axial-vector terms in Eq. (2.34), results in a different analysis procedure for Fig. 20a compared to Fig. 20b-c., similar behavior observed when analysing the vector parameter, ξ_V , and other parameters, ξ_A , ξ_S , and ξ_T , in the one-parameter scenario. These interference terms influence how the constraints are applied, which in turn affects the resulting bounds and the shape of the allowed regions in each scenario. In Fig. 20a, we display the allowed regions for COHERENT CsI(Na), and TEXONO pPC-Ge and nPC-Ge in the $\xi_V - \xi_A$ parameter space. For CsI, a broken-ellipse-shaped region is observed, centred around $\xi_V \approx 0.02$ and $\xi_V \approx 1.9$. Such regions typically arise when the contributions from the SM and exotic neutral interactions completely cancel each other out. However, no degenerate region is observed for both TEXONO experiments in this case.

In Fig. 20b, we present the allowed regions in the $\xi_V - \xi_S$ parameter space. Since we shift from the parameter-square space to the parameter space for ξ_S , only the positive region can be included. While the CO-

HERENT LAr exhibits half-elliptical bounds with a degeneracy region, symmetry breaking is observed in the COHERENT CsI similar to the pattern seen in Fig. 20a. However, this time only the left part of the broken ellipse remains. Next, we illustrate our limits in the $\xi_V - \xi_T$ parameter space in Fig. 20c. Here, a degeneracy region appears for both COHERENT CsI and LAr, taking the shape of a half-ellipse with thinner bounds as it approaches the top. These findings suggest that, with improved detector sensitivities or through combined analyses, it may be possible to break the degeneracies and achieve more stringent constraints. In the bottom panel of Fig. 20, we present the bounds for the $\xi_A - \xi_T$, $\xi_A - \xi_S$, and $\xi_T - \xi_S$ parameter spaces. Unlike the figures in the upper panel, these scenarios do not include SM interference or mutual interference between the parameters. The parameters in the χ^2 function appear in their second-order forms, which again necessitates the transition from parameter-squared space to parameter space. As a result, we observe only quarter-elliptical bounds without any degeneracy region. Additionally, for the $\xi_A - \xi_T$ and $\xi_A - \xi_S$ parameter spaces, we do not set limits for COHERENT LAr, as it has an even number of nucleon, as explained in previous sections. For TEXONO, all parameter spaces exhibit less stringent bounds compared to COHERENT, with no degeneracy regions present. Notably, TEXONO pPC-Ge results show a remarkable improvement over TEXONO nPC-Ge, demonstrating the potential of future reactor-based experiments to compete with accelerator-based experiments in exotic parameter spaces.

E. Overview of Our Results

In this work, we present a comprehensive analysis of NSI of neutrinos by comparing accelerator-based (COHERENT) and reactor-based (TEXONO) CE ν NS experiments, highlighting their complementary roles in probing NSI and the impact of detector advancements on parameter constraints. We focus on five different NSI interaction types: vector (V), axialvector (A), scalar (S), pseudoscalar (P) and tensor (T), and present the 90% CL exclusion bounds for key NSI parameters using a 1-bin analysis of the data from TEXONO nPC-Ge(2016) and pPC-Ge(2024), and COHERENT CsI(Na) and LAr experiments. Accelerator-based experiments operate at higher neutrino energies and larger momentum transfer (q^2) regime, and allow interactions with multiple neutrino flavors (ν_μ , $\bar{\nu}_\mu$, ν_e). This makes them particularly well-suited for investigating flavor-off-diagonal (FV) NSI scenarios, which require multiple neutrino flavors to effectively resolve potential new physics contributions. As seen in Figs. 9–11, COHERENT experiments generally provide tighter bounds than TEXONO, with a particularly large difference in the FV cases (e.g., Figs. 11a–h).

In contrast, reactor neutrino experiments operate at lower energies, offering several unique advantages for

flavor-diagonal (FC) NSI scenarios. In these cases, the difference between COHERENT and TEXONO constraints is less pronounced, such as the one shown in Fig. 9a, as reactor-based experiments, dominated by electron antineutrinos ($\bar{\nu}_e$), reduces flux uncertainties associated with the presence of multiple neutrino flavors in accelerator-based experiments. A similar trend is observed for other interaction types (see Figs. 14–19), except for the axial case (Figs. 12 and 13), where the significantly larger spin contribution from Ge target in TEXONO leads to tighter bounds compared to CsI(Na) target in COHERENT.

Besides, one of the key feature of this work is to present the first NSI analysis of TEXONO pPC-Ge (2024) data with a detector threshold of 200 eV. This advancement improves NSI constraints compared to the previous TEXONO nPC-Ge (2016) data and achieves results competitive with other reactor neutrino experiments. Furthermore, the low-energy nature of reactor neutrinos increases the sensitivity to the NSI model with light mediators, strengthening the constraints, especially in the low momentum transfer regime, where deviations from the Standard Model are more pronounced. As illustrated in Figure 8, except for the vector case, TEXONO pPC-Ge provides better upper limits than COHERENT and shows a significant improvement over TEXONO nPC-Ge.

Consistent with the model-independent NSI approach, exotic neutral-current interactions yield stronger constraints for COHERENT experiments than for TEXONO (as seen in Fig. 20). This reflects the advantage of accelerator-based experiments at higher energies and larger momentum transfers, further strengthening the role of CE ν NS in probing new physics BSM.

V. CONCLUSIONS

Different experimental setups, with varying thresholds and neutrino energy spectra, contribute to probing distinct regions of the NSI parameter space in CE ν NS. Reactor neutrinos, being emitted at lower energies, provide a more powerful probe for light mediator models. In contrast, the high-energy neutrinos from the SNS are better suited for exploring new physics associated with heavier mediators. This dual sensitivity underscores the complementarity of reactor- and SNS-based CE ν NS experiments in probing a wide range of mediator masses. This study provides a comprehensive analysis of NSI within the framework of CE ν NS, utilizing both the simplified model and model-independent approach, as well as exploring exotic neutral interactions.

We note that the studies of NSI with COHERENT CsI and LAr data have been pursued in previous works [48, 51, 53–55, 58, 60, 63–65]. In particular, we present the first NSI analysis based on TEXONO experiments, using both nPC-Ge data from 2016 and recently released pPC-Ge data from 2024. This enables a system-

atic evaluation of advancements in detector technology have increased NSI constraints, providing new insights into the evolving sensitivity of reactor neutrino experiments. Unlike many NSI studies that rely on new or older dataset(s), our work provides a complementary perspective by analysing COHERENT and TEXONO data, enabling a direct comparison of their constraints on NSI parameters – COHERENT probing accelerator-based neutrino interactions with multiple flavors at higher energies, while TEXONO focuses on a reactor neutrino environment dominated by electron antineutrinos at lower energies. Additionally, unlike many existing studies that focus on a limited set of interactions, such as only vector and scalar type interactions in simplified model or vector type interaction in model-independent NSI, our work includes a broader range of all possible interaction types in both simplified model and model-independent approach, as well as exotic neutral current interactions.

The abundance of neutrino sources that meet the detection criteria, including terrestrial sources, solar and atmospheric neutrinos as well as those from accelerators and nuclear power plants, is expected to drive in-

creased scientific activity in the near future. This work underscores the potential for future CE ν NS experiments to further probe NSI and enhance our understanding of new physics BSM. Moreover, we highlight that future improvements in detector sensitivities could resolve degeneracies and enable tighter constraints, particularly in two-parameter scenarios. Our results may also offer clue for the search for new mediators in the low-energy realm, likely driven by advancements in neutrino or DM experiments in the near future.

ACKNOWLEDGMENTS

This work is supported by the Investigator Award ASIA-106-M02 and Thematic Project AS-TP-112-M01 from the Academia Sinica, Taiwan, and contracts 106-2923-M-001-006-MY5, 107-2119-M-001-028-MY3 and 110-2112-M-001-029-MY3, 113-2112-M-001-053-MY3 from the National Science and Technology Council, Taiwan.

-
- [1] S. Navas *et al.* [Particle Data Group], “Review of particle physics”, *Phys. Rev. D* **110**, 030001 (2024).
- [2] D. Z. Freedman, “Coherent Neutrino Nucleus Scattering as a Probe of the Weak Neutral Current”, *Phys. Rev. D* **9**, 1389 (1974).
- [3] D. Z. Freedman, D. N. Schramm and D. L. Tubbs, “The Weak Neutral Current and its Effects in Stellar Collapse”, *Ann. Rev. Nucl. Part. Sci.* **27**, 167-207 (1977).
- [4] D. Akimov *et al.* [COHERENT Collaboration], “Observation of Coherent Elastic Neutrino-Nucleus Scattering”, *Science* **357**, 6356, 1123 (2017).
- [5] D. Akimov *et al.* [COHERENT Collaboration], “Measurement of the Coherent Elastic Neutrino-Nucleus Scattering Cross Section on CsI by COHERENT”, *Phys. Rev. Lett.* **129**, 8, 081801 (2022).
- [6] D. Akimov *et al.* [COHERENT Collaboration], “First Measurement of Coherent Elastic Neutrino-Nucleus Scattering on Argon”, *Phys. Rev. Lett.* **126**, 1, 012002 (2021).
- [7] S. Adamski *et al.* [COHERENT Collaboration], “First detection of coherent elastic neutrino-nucleus scattering on germanium”, [arXiv:2406.13806 (nucl-ex)].
- [8] S. J. Brice *et al.*, “A method for measuring coherent elastic neutrino-nucleus scattering at a far off-axis high-energy neutrino beam target”, *Phys. Rev. D* **89**, 072004 (2014).
- [9] H. Bonet *et al.* [CONUS Collaboration], “Constraints on Elastic Neutrino Nucleus Scattering in the Fully Coherent Regime from the CONUS Experiment”, *Phys. Rev. Lett.* **126**, 4, 041804 (2021).
- [10] N. Ackermann *et al.*, “First observation of reactor antineutrinos by coherent scattering”, [arXiv:2501.05206(hep-ex)].
- [11] H. T. Wong, H. B. Li, J. Li, Q. Yue, and Z. Y. Zhou, “Research program towards observation of neutrino-nucleus coherent scattering”, *J. Phys. Conf. Ser.* **39**, 266 (2006).
- [12] A. Aguilar-Arevalo *et al.* [CONNIE Collaboration], “Search for light mediators in the low-energy data of the CONNIE reactor neutrino experiment”, *J. High Energy Phys.* **2020**, 054 (2020).
- [13] J. Billard *et al.*, “Coherent neutrino scattering with low temperature bolometers at Chooz reactor complex”, *J. Phys. G: Nucl. Part. Phys.* **44**, 105101 (2017).
- [14] I. Alekseev *et al.* [ν GeN Collaboration], “First results of the ν GeN experiment on coherent elastic neutrino-nucleus scattering”, *Phys. Rev. D* **106**, L051101 (2022).
- [15] J. Colaresi, J. I. Collar, T. W. Hossbach, A. R. L. Kavner, C. M. Lewis, A. E. Robinson, and K. M. Yocum “First results from a search for coherent elastic neutrino-nucleus scattering at a reactor site”, *Phys. Rev. D* **104**, 072003 (2021).
- [16] “Background studies for the MINER Coherent Neutrino Scattering reactor experiment”, G. Agnolet *et al.* [MINER Collaboration], *Nucl. Instrum. Meth. A* **853**, 53 (2017).
- [17] S. Kerman *et al.*, “Coherency in neutrino-nucleus elastic scattering”, *Phys. Rev. D* **93**, 113006 (2016); V. Sharma *et al.* [TEXONO Collaboration], “Studies of quantum-mechanical coherency effects in neutrino-nucleus elastic scattering”, *Phys. Rev. D* **103**, 9, 092002 (2021).
- [18] E. Aprile *et al.* [XENON Collaboration], “Projected WIMP sensitivity of the XENONnT dark matter experiment”, *JCAP* **11**, 031 (2020).
- [19] J. Aalbers *et al.* [DARWIN Collaboration], “DARWIN: towards the ultimate dark matter detector”, *JCAP* **11**, 017 (2016).
- [20] D. S. Akerib *et al.* [LZ Collaboration], “The LUX-ZEPLIN (LZ) Experiment”, *Nucl. Instrum. Meth. A* **953**, 163047 (2020).
- [21] H. Zhang *et al.* [PandaX Collaboration], “Dark matter direct search sensitivity of the PandaX-4T experiment”,

- Sci. China Phys. Mech. Astron.* **62**, 3, 31011 (2019).
- [22] Zihao Bo *et al.* [PandaX Collaboration], “First Indication of Solar ^8B Neutrinos through Coherent Elastic Neutrino-Nucleus Scattering in PandaX-4T”, *Phys. Rev. Lett.* **133**, 191001 (2024).
- [23] E. Aprile *et al.* [XENON Collaboration], “First Indication of Solar ^8B Neutrinos via Coherent Elastic Neutrino-Nucleus Scattering with XENONnT”, *Phys. Rev. Lett.* **133**, 191002 (2024).
- [24] “Neutrino electromagnetic form factors”, P. Vogel and J. Engel, *Phys. Rev. D* **39**, 3378 (1989).
- [25] J. Billard, J. Johnston and B. J. Kavanagh, “Prospects for exploring New Physics in Coherent Elastic Neutrino-Nucleus Scattering”, *JCAP* **11**, 016 (2018).
- [26] O. G. Miranda, D. K. Papoulias, O. Sanders, M. Tórtola and J. W. F. Valle, “Future $\text{CE}\nu\text{NS}$ experiments as probes of lepton unitarity and light-sterile neutrinos”, *Phys. Rev. D* **102**, 113014 (2020).
- [27] M. Cadeddu, C. Giunti, Y. F. Li and Y. Y. Zhang, “Average CsI neutron density distribution from COHERENT data”, *Phys. Rev. Lett.* **120**, 7, 072501 (2018).
- [28] J. R. Wilson, “Coherent Neutrino Scattering and Stellar Collapse”, *Phys. Rev. Lett.* **32**, 849 (1974).
- [29] “Supernova observation via neutrino-nucleus elastic scattering in the CLEAN detector”, C. J. Horowitz, K. J. Coakley, and D. N. McKinsey, *Phys. Rev. D* **68**, 023005 (2003).
- [30] “Reactor Monitoring (near and far) with Neutrinos”, J. Learned, *Nucl. Phys. B, Proc. Suppl.* **143**, 152 (2005).
- [31] “Neutrino-nucleus coherent scattering as a probe of neutron density distributions”, K. Patton, J. Engel, G. C. McLaughlin, and N. Schunck, *Phys. Rev. C* **86**, 024612 (2012).
- [32] “Producing a new Fermion in Coherent Elastic Neutrino-Nucleus Scattering: from Neutrino Mass to Dark Matter”, V. Brdar, W. Rodejohann and X. J. Xu, *J. High Energy Phys.* **2018**, 024 (2018).
- [33] J. Liu, X. Chen and X. Ji, “Current status of direct dark matter detection experiments”, *Nature Phys.* **13**, 3, 212-216 (2017).
- [34] M. Schumann, “Direct Detection of WIMP Dark Matter: Concepts and Status”, *J. Phys. G* **46**, 10, 103003 (2019).
- [35] “Neutrino backgrounds to dark matter searches”, J. Monroe and P. Fisher, *Phys. Rev. D* **76**, 033007 (2007).
- [36] “Solar and atmospheric neutrinos: Background sources for the direct dark matter searches”, A. Gutlein *et al.*, *Astropart. Phys.* **34**, 90 (2010).
- [37] “Review of Particle Physics”, M. Drees and G. Gerbier, *Chin. Phys. C* **38**, 353 (2014), and references therein.
- [38] L. M. Krauss, “Low-energy neutrino detection and precision tests of the standard model”, *Phys. Lett. B* **269**, 407-411 (1991).
- [39] K. Scholberg, “Prospects for measuring coherent neutrino-nucleus elastic scattering at a stopped-pion neutrino source”, *Phys. Rev. D* **73**, 033005 (2006).
- [40] Juan Barranco, Omar G. Miranda, and Timur I. Rashba, “Probing new physics with coherent neutrino scattering off nuclei”, *J. High Energy Phys.* **12**, 021 (2005); J. Barranco, O. G. Miranda, and T. I. Rashba, “Sensitivity of low energy neutrino experiments to physics beyond the standard model”, *Phys. Rev. D* **76**, 073008 (2007).
- [41] Y. Farzan, M. Lindner, W. Rodejohann and X. J. Xu, “Probing neutrino coupling to a light scalar with coherent neutrino scattering”, *J. High Energy Phys.* **2018**, 066 (2018).
- [42] J. Barranco, A. Bolanos, E. A. Garcés, O. G. Miranda and T. I. Rashba, “Tensorial NSI and Unparticle physics in neutrino scattering”, *Int. J. Mod. Phys. A* **27**, 1250147 (2012).
- [43] M. A. Corona, M. Cadeddu, N. Cargioli, F. Dordei, and C. Giunti, “Reactor antineutrinos $\text{CE}\nu\text{NS}$ on germanium: CONUS+ and TEXONO as a new gateway to SM and BSM physics”, [arXiv:2501.18550(hep-ph)].
- [44] Manfred Lindner, Werner Rodejohann and Xun-Jie Xu, “Coherent neutrino-nucleus scattering and new neutrino interactions”, *J. High Energy Phys.*, **2017**, 97 (2017).
- [45] O. G. Miranda, and H. Nunokawa, “Non standard neutrino interactions: current status and future prospects”, *New J. Phys.* **17**, 095002 (2015).
- [46] M. Alpízar-Venegas, L. J. Flores, Eduardo Peinado, and E. Vázquez-Jáuregui, “Exploring the Standard Model and Beyond from the Evidence of $\text{CE}\nu\text{NS}$ with Reactor Antineutrinos in CONUS+”, [arXiv:2501.10355(hep-ph)].
- [47] A. Chattaraj, A. Majumdar, R. Srivastava, “Probing Standard Model and Beyond with Reactor $\text{CE}\nu\text{NS}$ Data of CONUS+ experiment”, [arXiv:2501.12441(hep-ph)].
- [48] D. K. Papoulias and T. S. Kosmas, “COHERENT constraints to conventional and exotic neutrino physics”, *Phys. Rev. D* **97**, No.3, 033003 (2018).
- [49] H. Bonet *et al.* [CONUS Collaboration], “Novel constraints on neutrino physics beyond the standard model from the CONUS experiment”, *J. High Energy Phys.* **2022**, 85 (2022).
- [50] A. Aguilar-Arevalo *et al.* [CONNIE Collaboration], “Search for light mediators in the low-energy data of the CONNIE reactor neutrino experiment”, *J. High Energy Phys.* **2020**, 54 (2020).
- [51] O. G. Miranda, D. K. Papoulias, G. S. Garcia, O. Sanders, M. Tortola, and J. W. Valle, “Implications of the first detection of coherent elastic neutrino-nucleus scattering ($\text{CE}\nu\text{NS}$) with Liquid Argon”, *J. High Energy Phys.* **2020**, 130 (2020).
- [52] J. Liao, H. Liu, and D. Marfatia, “Implications of the first evidence for coherent elastic scattering of reactor neutrinos”, *Phys. Rev. D* **106**(3), L031702 (2022).
- [53] M. A. Corona, M. Cadeddu, N. Cargioli, F. Dordei, C. Giunti, Y. F. Li, E. Picciau, C. A. Ternes, and Y. Y. Zhang, “Probing light mediators and $(g-2)\mu$ through detection of coherent elastic neutrino nucleus scattering at COHERENT”, *J. High Energy Phys.*, **2022**, 109, (2022).
- [54] P. Coloma, I. Esteban, M. C. Gonzalez-Garcia, L. Larizgoitia, F. Monrabal, and S. Palomares-Ruiz, “Bounds on new physics with data of the Dresden-II reactor experiment and COHERENT”, *J. High Energy Phys.* **2022**, 37 (2022).
- [55] M. Cadeddu, N. Cargioli, F. Dordei, C. Giunti, Y. F. Li, E. Picciau, and Y. Y. Zhang, “Constraints on light vector mediators through coherent elastic neutrino-nucleus scattering data from COHERENT”, *J. High Energy Phys.* **2021**, 116 (2021).
- [56] M. Lindner, T. Rink, and M. Sen, “Light vector bosons and the weak mixing angle in the light of new reactor-based $\text{CE}\nu\text{NS}$ experiments”, *J. High Energy Phys.* **2024**, 171 (2024).
- [57] M. Demirci and M. F. Mustamin, “Solar neutrino constraints on light mediators through coherent elastic

- neutrino-nucleus scattering”, *Phys. Rev. D* **109**, 015021 (2024).
- [58] C. Giunti, “General COHERENT constraints on neutrino nonstandard interactions”, *Phys. Rev. D* **101**, 3, 035039 (2020).
- [59] M. F. Mustamin and M. Demirci, “Study of Non-standard Neutrino Interactions in Future Coherent Elastic Neutrino-Nucleus Scattering Experiments”, *Braz. J. Phys.* **51**, 3, 813-819 (2021).
- [60] S. S. Chatterjee, S. Lavignac, O. G. Miranda, and G. S. Garci, “Exploring the sensitivity to non-standard neutrino interactions of NaI and cryogenic CsI detectors at the Spallation Neutron Source”, *Phys. Rev. D* **110**(9),095027 (2024).
- [61] S. S. Chatterjee, S. Lavignac, O. G. Miranda, and G. Sanchez Garcia, “Constraining nonstandard interactions with coherent elastic neutrino-nucleus scattering at the European Spallation Source”, *Phys. Rev. D* **107**,055019 (2023).
- [62] B. C. Canas, E. A. Garces, O. G. Miranda, A. Parada, G. Sanchez Garcia, “Interplay between nonstandard and nuclear constraints in coherent elastic neutrino-nucleus scattering experiments”, *Phys. Rev. D* **101**, 035012 (2020).
- [63] D. Aristizabal Sierra, V. De Romeri and N. Rojas, “COHERENT analysis of neutrino generalized interactions”, *Phys. Rev. D* **98**, 075018 (2018).
- [64] L. J. Flores, Newton Nath, and Eduardo Peinado, “CE ν NS as a probe of flavored generalized neutrino interactions”, *Phys. Rev. D* **105**, 055010 (2022).
- [65] V. De Romeri, O. G. Miranda, D. K. Papoulias, G. Sanchez Garcia, M. Tórtola, and J. W. Valle, “Physics implications of a combined analysis of COHERENT CsI and LAr data”, *J. High Energy Phys.* **2023**, 35 (2023).
- [66] R. Abbasi *et al.* [IceCube Collaboration], “All-flavor constraints on nonstandard neutrino interactions and generalized matter potential with three years of IceCube DeepCore data”, *Phys. Rev. D* **104**(7), 072006 (2021).
- [67] A. Kumar *et al.*, “A new approach to probe non-standard interactions in atmospheric neutrino experiments”, *J. High Energy Phys.* **2021**, 159 (2021).
- [68] B. Dev *et al.*, “Neutrino non-standard interactions: A status report”, *SciPost Phys. Proc.* **2**, 001 (2019).
- [69] D. Aristizabal Sierra, N. Rojas and M. H. G. Tytgat, “Neutrino non-standard interactions and dark matter searches with multi-ton scale detectors”, *J. High Energy Phys.* **2018**, 197 (2018).
- [70] J. C. Park, G. Tomar, “Probing Non-Standard Neutrino Interactions with Interference: Insights from Dark Matter and Neutrino Experiments”, *JCAP* **08**(2023)025.
- [71] V. D. Romeri, D. K. Papoulias, and G. S. Garcia, “Implications of the first CONUS+ measurement of coherent elastic neutrino-nucleus scattering”, [[arXiv:2501.17843](https://arxiv.org/abs/2501.17843) (hep-ph)].
- [72] I. Bischer and W. Rodejohann, “General neutrino interactions from an effective field theory perspective”, *Nucl. Phys. B* **947**, 114746 (2019).
- [73] C. D. McCoy and M. Massimi, “Simplified models: a different perspective on models as mediators”, *Euro. Jnl. Phil. Sci.* **8**, 99-123 (2018).
- [74] J. Erler, and M. J. Ramsey-Musolf, “Weak mixing angle at low energies”, *Phys. Rev. D* **72**, 073003 (2005).
- [75] G. Belanger, F. Boudjema, A. Pukhov, and A. Semenov, “micrOMEGAs3.1 : a program for calculating dark matter observables”, *Computer Physics Communications* **185**(3), 960-985.(2014).
- [76] A. Majumdar, D. K. Papoulias, and R. Srivastava, “Dark matter detectors as a novel probe for light new physics”, *Physical Review D* **106**(1), 013001 (2022).
- [77] M. Hoferichter, J. Menéndez, and A. Schwenk, “Coherent elastic neutrino-nucleus scattering: EFT analysis and nuclear responses”, *Physical Review D* **102**(7), 074018(2020).
- [78] R. H. Helm, “Inelastic and Elastic Scattering of 187-Mev Electrons from Selected Even-Even Nuclei”, *Phys. Rev.* **104**, 1466-1475 (1956).
- [79] G. Duda, A. Kemper and P. Gondolo, “Model Independent Form Factors for Spin Independent Neutralino-Nucleon Scattering from Elastic Electron Scattering Data”, *JCAP* **04**, 012 (2007).
- [80] D. G. Cerdeño, M. Fairbairn, T. Jubb, P. A. N. Machado, A. C. Vincent and C. Boehm, “Physics from solar neutrinos in dark matter direct detection experiments”, *J. High Energy Phys.* **2016**, 188 (2016) [erratum: *J. High Energy Phys.* **2016**, 048 (2016)]
- [81] J. Abdallah *et al.*, “Simplified models for dark matter searches at the LHC”, *Phys. Dark Univ.* **9-10**, 8 (2015).
- [82] J. B. Dent, B. Dutta, S. Liao, J. L. Newstead, L. E. Strigari and J. W. Walker, “Probing light mediators at ultralow threshold energies with coherent elastic neutrino-nucleus scattering”, *Phys. Rev. D* **96**, 9, 095007 (2017).
- [83] Y. Ema, F. Sala and R. Sato, “Neutrino experiments probe hadrophilic light dark matter”, *SciPost Phys.* **10**, 072 (2021).
- [84] S. Davidson, C. Pena-Garay, N. Rius, and A. Santamaria, “Present and future bounds on non-standard neutrino interactions”, *J. High Energy Phys.*, **03**, 011 (2003).
- [85] Z. Berezhiani, and A. Rossi, “Limits on the non-standard interactions of neutrinos from e+e- colliders”, *Phys. Lett. B*, **535**, 207-218 (2002).
- [86] Y. Farzan, and I. M. Shoemaker, “Lepton flavor violating non-standard interactions via light mediators”, *J. High Energy Phys.*, **2016**, 33 (2016).
- [87] F. T. Avignone and Yu. V. Efremenko, “Neutrino-nucleus cross-section measurements at intense, pulsed spallation sources”, *J. Phys. G: Nucl. Part. Phys.* **29**, 2615 (2003).
- [88] D. Akimov *et al.* [COHERENT Collaboration], “The COHERENT Experiment at the Spallation Neutron Source”, [arXiv:1509.08702](https://arxiv.org/abs/1509.08702) (2015), and references therein.
- [89] J. N. Bahcall and M. H. Pinsonneault, “What do we (not) know theoretically about solar neutrino fluxes?”, *Phys. Rev. Lett.* **92**, 121301 (2004).
- [90] G. Battistoni, A. Ferrari, T. Montaruli and P. R. Sala, “The atmospheric neutrino flux below 100-MeV: The FLUKA results”, *Astropart. Phys.* **23**, 526-534 (2005).
- [91] J. I. Collar, N. E. Fields, M. Hai, T. W. Hossbach, J. L. Orrell, C. T. Overman, G. Perumpilly, and B. Scholz, “Coherent neutrino-nucleus scattering detection with a CsI[Na] scintillator at the SNS spallation source”, *Nucl. Instrum. Methods Phys. Res., Sect. A* **773**, 56 (2015), and Supplemental Material.
- [92] H. T. Wong *et al.*, “Search of neutrino magnetic moments with a high-purity germanium detector at the Kuo-Sheng nuclear power station”, *Phys. Rev. D* **75**, 012001 (2007).
- [93] A. K. Soma, M. K. Singh, L. Singh, L. T. Yang, W. Zhao, M. Agartioglu, G. Asryan, Y. Y. Chang, J. H. Chen, Y. C. Chuang, M. Deniz, M. Zeyrek [TEXONO Collab-

- oration], “Characterization and performance of germanium detectors with sub-keV sensitivities for neutrino and dark matter experiments”, *Nucl. Instrum. Methods Phys. Res., Sect. A* **836**, 67 (2016).
- [94] S. Karmakar *et al.* [TEXONO Collaboration], “New Limits on Coherent Neutrino Nucleus Elastic Scattering Cross Section at the Kuo-Sheng Reactor Neutrino Laboratory.”, [[arXiv:2411.18812](https://arxiv.org/abs/2411.18812)(nucl-ex)].
- [95] J. D. Lewin and P. F. Smith, “Review of mathematics, numerical factors, and corrections for dark matter experiments based on elastic nuclear recoil”, *Astropart. Phys.* **6**, 87 (1996).
- [96] Jiajun Liao, Hongkai Liu, and Danny Marfatia, “Implications of the first evidence for coherent elastic scattering of reactor neutrinos”, *Phys. Rev. D* **106**, L031702 (2022).
- [97] J. Colaresi, J. I. Collar, T. W. Hossbach, C. M. Lewis, and K. M. Yocum, “Measurement of Coherent Elastic Neutrino-Nucleus Scattering from Reactor Antineutrinos”, *Phys. Rev. Lett.- Supplemental Material* **129**, 211802 (2022).
- [98] I. Bischer and W. Rodejohann, “General neutrino interactions at the DUNE near detector.”, *Phys. Rev. D* **99**(3), 036006(2019).

TABLE IV. Summary of best fit results and corresponding limits at 90% CL for vector, axialvector, scalar, pseudoscalar, and tensor NSI measurements for one parameter at a time analysis for COHERENT CsI(Na) and COHERENT LAr experiments. Here only coupling parameter is assumed to be non-zero for each bound.

Fitting Par	COHERENT CsI(Na)			COHERENT LAr		
	BFPV $\pm 1\sigma$	90% CL	χ^2/dof	BFPV $\pm 1\sigma$	90% CL	χ^2/dof
ε_{ee}^{uV}	0.015 ± 0.0385 0.355 ± 0.0385	$[-0.039, 0.097]$ & $[0.273, 0.409]$	3.83/8	0.0197 ± 0.243	$[-0.10, 0.465]$	5.47/5
ε_{ee}^{dV}	0.014 ± 0.036 0.33 ± 0.0365	$[-0.036, 0.090]$ & $[0.254, 0.380]$	3.83/8	0.0184 ± 0.0228	$[-0.094, 0.435]$	5.47/5
$\varepsilon_{\mu\mu}^{uV}$	0.0070 ± 0.0185 0.363 ± 0.0186	$[-0.021, 0.040]$ & $[0.329, 0.391]$	3.85/8	0.013 ± 0.0475 0.352 ± 0.0475	$[-0.0498, 0.124]$ & $[0.241, 0.414]$	5.42/5
$\varepsilon_{\mu\mu}^{dV}$	0.0065 ± 0.0172 0.337 ± 0.0173	$[-0.0196, 0.0375]$ & $[0.306, 0.363]$	3.85/8	0.0123 ± 0.0445 0.329 ± 0.044	$[-0.047, 0.116]$ & $[0.225, 0.388]$	5.42/5
$(\varepsilon_{e\mu}^{uV})^2$	-0.0017 ± 0.0044	$\varepsilon_{e\mu}^{uV} < 0.0738$	3.84/8	-0.0028 ± 0.0104	$\varepsilon_{e\mu}^{uV} < 0.120$	5.44/5
$(\varepsilon_{e\mu}^{dV})^2$	-0.0015 ± 0.0038	$\varepsilon_{e\mu}^{dV} < 0.0686$	3.84/8	-0.0025 ± 0.0091	$\varepsilon_{e\mu}^{dV} < 0.112$	5.44/5
$(\varepsilon_{e\tau}^{uV})^2$	-0.0053 ± 0.0129	$\varepsilon_{e\tau}^{uV} < 0.127$	3.83/8	-0.0068 ± 0.0324	$\varepsilon_{e\tau}^{uV} < 0.216$	5.47/5
$(\varepsilon_{e\tau}^{dV})^2$	-0.0045 ± 0.0111	$\varepsilon_{e\tau}^{dV} < 0.117$	3.83/8	-0.0059 ± 0.0285	$\varepsilon_{e\tau}^{dV} < 0.202$	5.47/5
$(\varepsilon_{\mu\tau}^{uV})^2$	-0.0025 ± 0.0066	$\varepsilon_{\mu\tau}^{uV} < 0.0908$	3.85/8	-0.0046 ± 0.0154	$\varepsilon_{\mu\tau}^{uV} < 0.144$	5.42/5
$(\varepsilon_{\mu\tau}^{dV})^2$	-0.0022 ± 0.0057	$\varepsilon_{\mu\tau}^{dV} < 0.0844$	3.85/8	-0.0040 ± 0.0134	$\varepsilon_{\mu\tau}^{dV} < 0.135$	5.42/5
$(\varepsilon_{ee(\tau)}^{uA})^2$	-7840.0 ± 11870	$\varepsilon_{ee(\tau)}^{uA} < 108.12$	3.55/8	—	—	—
$(\varepsilon_{ee(\tau)}^{dA})^2$	-149.80 ± 226.80	$\varepsilon_{ee(\tau)}^{dA} < 14.947$	3.55/8	—	—	—
$(\varepsilon_{\mu\mu(\tau)}^{uA})^2$	-3730.0 ± 5505.0	$\varepsilon_{\mu\mu(\tau)}^{uA} < 72.938$	3.53/8	—	—	—
$(\varepsilon_{\mu\mu(\tau)}^{dA})^2$	-71.40 ± 105.10	$\varepsilon_{\mu\mu(\tau)}^{dA} < 10.079$	3.53/8	—	—	—
$(\varepsilon_{e\mu}^{uA})^2$	-2580.0 ± 3800.0	$\varepsilon_{e\mu}^{uA} < 60.581$	3.52/8	—	—	—
$(\varepsilon_{e\mu}^{dA})^2$	-49.30 ± 72.50	$\varepsilon_{e\mu}^{dA} < 8.373$	3.52/8	—	—	—
$(\varepsilon_{ee(\tau)}^{uS})^2$	$(-3.76 \pm 5.19) \times 10^{-4}$	$\varepsilon_{ee(\tau)}^{uS} < 0.0219$	3.47/8	$(-1.00 \pm 19.2) \times 10^{-4}$	$\varepsilon_{ee(\tau)}^{uS} < 0.055$	5.51/5
$(\varepsilon_{ee(\tau)}^{dS})^2$	$(-5.22 \pm 7.24) \times 10^{-4}$	$\varepsilon_{ee(\tau)}^{dS} < 0.0259$	3.47/8	$(-1.40 \pm 26.2) \times 10^{-4}$	$\varepsilon_{ee(\tau)}^{dS} < 0.065$	5.51/5
$(\varepsilon_{\mu\mu(\tau)}^{uS})^2$	$(-1.76 \pm 2.36) \times 10^{-4}$	$\varepsilon_{\mu\mu(\tau)}^{uS} < 0.0146$	3.43/8	$(-1.40 \pm 9.00) \times 10^{-4}$	$\varepsilon_{\mu\mu(\tau)}^{uS} < 0.037$	5.49/5
$(\varepsilon_{\mu\mu(\tau)}^{dS})^2$	$(-2.46 \pm 3.29) \times 10^{-4}$	$\varepsilon_{\mu\mu(\tau)}^{dS} < 0.0172$	3.43/8	$(-2.00 \pm 12.4) \times 10^{-4}$	$\varepsilon_{\mu\mu(\tau)}^{dS} < 0.043$	5.49/5
$(\varepsilon_{e\mu}^{uS})^2$	$(-1.24 \pm 1.65) \times 10^{-4}$	$\varepsilon_{e\mu}^{uS} < 0.0122$	3.43/8	$(-0.78 \pm 6.11) \times 10^{-4}$	$\varepsilon_{e\mu}^{uS} < 0.031$	5.50/5
$(\varepsilon_{e\mu}^{dS})^2$	$(-1.72 \pm 2.30) \times 10^{-4}$	$\varepsilon_{e\mu}^{dS} < 0.0144$	3.43/8	$(-1.06 \pm 8.38) \times 10^{-4}$	$\varepsilon_{e\mu}^{dS} < 0.036$	5.50/5
$(\varepsilon_{ee(\tau)}^{uP})^2$	-1.274 ± 1.46	$\varepsilon_{ee(\tau)}^{uP} < 1.061$	3.23/8	-0.097 ± 0.641	$\varepsilon_{ee(\tau)}^{uP} < 0.979$	5.49/5
$(\varepsilon_{ee(\tau)}^{dP})^2$	-28.84 ± 33.0	$\varepsilon_{ee(\tau)}^{dP} < 5.048$	3.23/8	-2.14 ± 14.16	$\varepsilon_{ee(\tau)}^{dP} < 4.601$	5.49/5
$(\varepsilon_{\mu\mu(\tau)}^{uP})^2$	-0.72 ± 0.73	$\varepsilon_{\mu\mu(\tau)}^{uP} < 0.689$	3.01/8	-0.137 ± 0.331	$\varepsilon_{\mu\mu(\tau)}^{uP} < 0.639$	5.34/5
$(\varepsilon_{\mu\mu(\tau)}^{dP})^2$	-16.3 ± 16.43	$\varepsilon_{\mu\mu(\tau)}^{dP} < 3.277$	3.01/8	-3.02 ± 7.32	$\varepsilon_{\mu\mu(\tau)}^{dP} < 3.003$	5.34/5
$(\varepsilon_{e\mu}^{uP})^2$	-0.476 ± 0.492	$\varepsilon_{e\mu}^{uP} < 0.578$	3.06/8	-0.071 ± 0.219	$\varepsilon_{e\mu}^{uP} < 0.538$	5.41/5
$(\varepsilon_{e\mu}^{dP})^2$	-10.76 ± 11.14	$\varepsilon_{e\mu}^{dP} < 2.750$	3.06/8	-1.57 ± 4.84	$\varepsilon_{e\mu}^{dP} < 2.528$	5.41/5
$(\varepsilon_{ee(\tau)}^{uT})^2$	-0.0175 ± 0.0311	$\varepsilon_{ee(\tau)}^{uT} < 0.183$	3.68/8	-0.0136 ± 0.0873	$\varepsilon_{ee(\tau)}^{uT} < 0.361$	5.49/5
$(\varepsilon_{ee(\tau)}^{dT})^2$	-0.008 ± 0.0143	$\varepsilon_{ee(\tau)}^{dT} < 0.125$	3.68/8	-0.0068 ± 0.0434	$\varepsilon_{ee(\tau)}^{dT} < 0.254$	5.49/5
$(\varepsilon_{\mu\mu(\tau)}^{uT})^2$	-0.0085 ± 0.0149	$\varepsilon_{\mu\mu(\tau)}^{uT} < 0.127$	3.67/8	-0.0105 ± 0.0411	$\varepsilon_{\mu\mu(\tau)}^{uT} < 0.239$	5.45/5
$(\varepsilon_{\mu\mu(\tau)}^{dT})^2$	-0.0039 ± 0.0069	$\varepsilon_{\mu\mu(\tau)}^{dT} < 0.086$	3.67/8	-0.0052 ± 0.0204	$\varepsilon_{\mu\mu(\tau)}^{dT} < 0.168$	5.45/5
$(\varepsilon_{e\mu}^{uT})^2$	-0.0058 ± 0.0101	$\varepsilon_{e\mu}^{uT} < 0.104$	3.67/8	-0.0062 ± 0.0279	$\varepsilon_{e\mu}^{uT} < 0.200$	5.46/5
$(\varepsilon_{e\mu}^{dT})^2$	-0.0026 ± 0.0047	$\varepsilon_{e\mu}^{dT} < 0.071$	3.67/8	-0.0031 ± 0.0139	$\varepsilon_{e\mu}^{dT} < 0.141$	5.46/5

TABLE V. Summary of the best-fit results and corresponding upper bounds at 90% CL in exotic neutral current interactions of $CE\nu NS$ measurements for exotic coupling constant parameters with ξ_X . The results are presented in comparison with two datasets from the TEXONO Collaboration: the 2016 dataset obtained with the nPC-Ge detector and the 2024 dataset obtained with the pPC-Ge detector. Here only one coupling parameter is assumed to be non-zero for each bound.

Fitting Par	TEXONO nPC-Ge			TEXONO pPC-Ge		
	BFPV $\pm 1\sigma$	90% CL	χ^2/dof	BFPV $\pm 1\sigma$	90% CL	χ^2/dof
ξ_V	0.96 ± 8.06	$[-9.79, 11.7]$	81.4/120	$0.004^{+2.71}_{-0.79}$	$[-1.146, 3.074]$	87.87/79
ξ_A^2	-0.86 ± 3.97	$\xi_A < 2.38$	81.3/120	0.009 ± 0.162	$\xi_A < 0.524$	87.86/79
ξ_S^2	-0.90 ± 4.18	$\xi_S < 2.44$	81.3/120	0.011 ± 0.175	$\xi_S < 0.546$	87.86/79
ξ_T^2	-3.03 ± 13.8	$\xi_T < 4.44$	81.3/120	0.024 ± 0.528	$\xi_T < 0.946$	87.86/79

TABLE VI. Summary of best-fit results and corresponding upper bounds at 90% CL for exotic coupling constant parameters of ξ_X in exotic interactions of $CE\nu NS$ for COHERENT CsI(Na) and LAr experiments. Here only one coupling parameter is assumed to be non-zero for each bound.

Fitting Par	COHERENT - CsI(Na)			COHERENT - LAr		
	BFPV $\pm 1\sigma$	90% CL	χ^2/dof	BFPV $\pm 1\sigma$	90% CL	χ^2/dof
ξ_V	0.025 ± 0.063 1.90 ± 0.063	$[-0.074, 0.135]$ & $[1.79, 2.00]$	3.8/8	0.042 ± 0.16 1.88 ± 0.16	$[-0.19, 0.355]$ & $[1.57, 2.12]$	5.4/5
ξ_A^2	-0.018 ± 0.027	$\xi_A < 0.160$	3.5/8	—	—	—
ξ_S^2	-0.025 ± 0.034	$\xi_S < 0.174$	3.4/8	-0.016 ± 0.12	$\xi_S < 0.433$	5.5/5
ξ_T^2	-0.036 ± 0.064	$\xi_T < 0.262$	3.7/8	-0.042 ± 0.19	$\xi_T < 0.517$	5.5/5